The Astrophysical Journal, 906:76 (21pp), 2021 January 10 https://doi.org/10.3847/1538-4357/abc882

Multiple Stellar Populations along the Red Horizontal Branch and Red Clump of Globular Clusters

E. Dondoglio[1], A. P. Milone[1,2], E. P. Lagioia[1], A. F. Marino[1,2,3,4], M. Tailo[1], G. Cordoni[1], S. Jang[1,5], and M. Carlos[6]

[1] Dipartimento di Fisica e Astronomia "Galileo Galilei," Università di Padova, Vicolo dell'Osservatorio 3, I-35122, Padua, Italy; emanuele.dondoglio@studenti.unipd.it
[2] Istituto Nazionale di Astrofisica—Osservatorio Astronomico di Padova, Vicolo dell'Osservatorio 5, I-35122, Padua, Italy
[3] Centro di Ateneo di Studi e Attività Spaziali "Giuseppe Colombo"—CISAS, via Venezia 15, I-35131, Padua, Italy
[4] INAF—Osservatorio Astrofisico di Arcetri, Largo E. Fermi, 5, 50125 Firenze, Italy
[5] Center for Galaxy Evolution Research and Department of Astronomy, Yonsei University, Seoul 03722, Republic of Korea
[6] Departamento de Astronomia, IAG, Universidade de São Paulo, Rua do Matão 1226, 05509-900 São Paulo, Brazil
Received 2020 August 4; revised 2020 October 23; accepted 2020 November 5; published 2021 January 11

Abstract

We exploit multiband Hubble Space Telescope photometry to investigate multiple populations (MPs) along the red horizontal branches (HBs) and red clumps of 14 metal-rich globular clusters (GCs), including 12 Milky Way GCs and the Magellanic Cloud GCs NGC 1978 and NGC 416. Based on appropriate two-color diagrams, we find that the fraction of first-generation (1G) stars in Galactic GCs correlates with cluster mass, confirming previous results based on red-giant branch (RGB) stars. Magellanic Cloud GCs show higher fractions of 1G stars than Galactic GCs with similar masses, thus suggesting that the environment affects the MP phenomenon. We compared and combined our population fractions based on the HB with previous estimates from the MS and RGB, and we used ground-based UBVI photometry (available for NGC 104, NGC 5927, NGC 6366, and NGC 6838) to extend the investigation over a wide field of view. All studied GCs are consistent with flat distributions of 1G and second-generation (2G) stars within $\sim 1'$ from the cluster center except NGC 416, where the 2G is more centrally concentrated. 2G stars of NGC 104 and NGC 5927 are more centrally concentrated than the 1G stars, whereas the distribution is flat for NGC 6366 and NGC 6838. We discover that most of the analyzed GCs exhibit extended sequences of 1G stars along the red HB, not consistent with a simple population. The comparison between appropriate synthetic and observed CMDs reveals that these extended distributions are consistent with either star-to-star variation in helium or with an internal metallicity spread, recalling the inhomogeneity of 1G stars along the chromosome maps.

Unified Astronomy Thesaurus concepts: Globular star clusters (656); Population II stars (1284); Chemical abundances (224); HST photometry (756); Magellanic Clouds (990)

1. Introduction

Multiband Hubble Space Telescope (HST) photometry revealed that the color–magnitude diagram (CMD) of most globular clusters (GCs) is composed of two main stellar populations that can be identified along the main evolutionary stages (e.g., Milone et al. 2012). One population, dubbed first generation (1G), is composed of stars with the same chemical composition of halo field stars with similar metallicity, while the remaining stars are enhanced in helium, nitrogen and sodium and depleted in carbon and oxygen and are named second generation (2G, e.g., Kraft 1994; Carretta et al. 2009; Marino et al. 2019a).

Studies based on pseudo-two-color diagrams called chromosome maps (ChMs) from homogeneous HST photometry of 59 Milky Way GCs revealed that the fraction of 1G stars and the internal variations of helium and nitrogen depend on cluster mass, thus indicating that the complexity of the multiple-population phenomenon is associated with the GC mass (Milone et al. 2017; Zennaro et al. 2019). The fraction of 1G stars of some Magellanic Cloud GCs can be even higher than that observed in Galactic GCs, which suggests that the properties of the multiple populations depend on the host galaxy (Lagioia et al. 2019b; Milone et al. 2020a). Intriguingly, 1G stars define extended sequences along the ChMs of many GCs, which may imply that they host stars with different chemical compositions (Milone et al. 2015, 2017). Star-to-star variations in metallicity and helium are possible responsible for the color extension of 1G stars of some GCs, but a comprehensive solution is still missing (e.g., Milone et al. 2015; D'Antona et al. 2016; Marino et al. 2019b; Tailo et al. 2019a).

These studies are typically based either on red-giant branch (RGB) or main-sequence (MS) stars. Although the horizontal branch (HB) is rarely used to derive accurate determinations of the relative numbers of 1G and 2G stars, it would provide unique information on multiple populations in GCs.

Early evidence of stellar populations with different chemical compositions along the red HB of GCs is provided by Norris & Freeman (1982), who combined photometry and spectroscopy of 14 stars of NGC 104 (47 Tuc) and detected bimodal CN distribution and C–N anticorrelation. A similar behavior has also been observed in NGC 6838 by Smith & Penny (1989). More recently, high-resolution spectroscopy has provided direct evidence that in GCs with intermediate metallicities ([Fe/H] ~ -1.0–1.4), Na-poor and O-rich stars populate the reddest part of the HB, while Na-rich and O-poor stars are mostly located on the blue HB (e.g., Marino et al. 2011, 2014).

In some GCs with intermediate metallicities, the red HB can host multiple populations with different light-element abundances that are merely mixed in the photometric diagrams (e.g.,

Table 1
Summary of the Data of NGC 416 and NGC 1978 Used in This Work

Date	$N \times$ EXPTIME	Filter	Instrument	Program	PI
		NGC 416			
2019 Jun 18	1500s+1512s+2 × 1529s+2 × 1525s	F275W	UVIS/WFC3	15630	N. Bastian
2019 Jul 31	1530s+1500s+2 × 1533s+2 × 1534s	F275W	UVIS/WFC3	15630	N. Bastian
2019 Aug 05	2 × 1500s+1512s+2 × 1515s+1523s	F275W	UVIS/WFC3	15630	N. Bastian
2016 Jun 16	700s+1160s+1200s	F336W	UVIS/WFC3	14069	N. Bastian
2016 Jun 16	500s+800s+1650s+1655s	F343N	UVIS/WFC3	14069	N. Bastian
2016 Jun 16	75s+150s+440s+460s	F438W	UVIS/WFC3	14069	N. Bastian
2005 Nov 22	2 × 20s	F555W	ACS/WFC	10396	J. Gallagher
2006 Mar 08	2 × 20s+4 × 496s	F555W	ACS/WFC	10396	J. Gallagher
2005 Nov 22	2 × 10s+4 × 474s	F814W	ACS/WFC	10396	J. Gallagher
2006 Mar 08	2 × 10s+4 × 474s	F814W	ACS/WFC	10396	J. Gallagher
		NGC 1978			
2019 Sep 17	2 × 1493s+2 × 1498s+2 × 1500s+2 × 1499s 1501s+1502s+1495s+1492s	F275W	UVIS/WFC3	15630	N. Bastian
2011 Aug 15	380s+460s	F336W	UVIS/WFC3	12257	L. Girardi
2016 Sep 25	660s+740s	F336W	UVIS/WFC3	14069	N. Bastian
2016 Sep 25	425s+450s+500s+2 × 800s+1000s	F343N	UVIS/WFC3	14069	N. Bastian
2016 Sep 25	75s+120s+420s+460s+650s+750s	F438W	UVIS/WFC3	14069	N. Bastian
2003 Oct 07	300s	F555W	ACS/WFC	9891	G. Gilmore
2011 Aug 15	60s+300s+680s	F555W	ACS/WFC	12257	L. Girardi
2003 Oct 07	200s	F814W	ACS/WFC	9891	G. Gilmore

Gratton et al. 2011; Marino et al. 2014). On the contrary, distinct sequences of 1G and 2G stars can be detected along the red HB of metal-rich GCs with [Fe/H] $\gtrsim -1.0$ by means of appropriate photometric diagrams. Milone et al. (2012) have shown that 1G red HB stars have redder $m_{\rm F275W} - m_{\rm F336W}$ colors than 2G red HB stars with the same $m_{\rm F336W} - m_{\rm F438W}$ color. As a consequence, the $m_{\rm F275W} - m_{\rm F336W}$ versus $m_{\rm F336W} - m_{\rm F438W}$ two-color diagram is a powerful tool to identify stellar populations along the red HB of metal-rich GCs. Photometric diagrams obtained from the appropriate combination of U, B, I magnitudes (Marino et al. 2008; Sbordone et al. 2011, e.g.,) or from the so-called JWL indices (Lee 2017, 2018, 2019) are exquisite tools to identify multiple populations among giant stars by using ground-based telescopes and have allowed split red HBs in some GCs, including 47 Tuc and NGC 6838 (e.g., Milone et al. 2012; Monelli et al. 2013; Lee & Sneden 2020; Cordoni et al. 2020), to be detected. In this work, we exploit multiband HST photometry of the Large Magellanic Cloud (LMC) GC NGC 1978, of the GC NGC 416 in the Small Magellanic Cloud (SMC) and of 12 Galactic GCs, namely NGC 104, NGC 5927, NGC 6304, NGC 6352, NGC 6366, NGC 6388, NGC 6441, NGC 6496, NGC 6624, NGC 6637, NGC 6652, and NGC 6838.

The paper is organized as follows. In Section 2, we describe the data set and data reduction. The photometric diagrams of red HB stars are presented in Section 3 where we investigate multiple populations along the red HB and derive the fraction of 1G stars. Section 4 investigates the relations between the fraction of 1G stars and the main parameters of the host clusters. In Section 5, we present the discovery of extended HB sequences for 1G stars of several GCs, while Section 6 is focused on the radial distributions of multiple populations. Finally, the summary and discussions are provided in Section 7.

2. Data and Data Reduction

To investigate the stellar populations along the HB in Galactic GCs, we used the photometric catalogs by Anderson et al. (2008), Milone et al. (2012, 2017), and Milone et al. (2018b), which provide astrometry and differential-reddening-corrected photometry in the F275W, F336W, and F438W bands of the Ultraviolet and Visual Channel of the Wide Field Camera 3 (UVIS/WFC3) on board HST and in the F606W and F814W bands of the Wide Field Channel of the Advanced Camera for Survey (ACS/WFC). To study the stellar populations in the GCs NGC 1978 and NGC 416, we derived stellar positions and multiband photometry by using the archive HST images summarized in Table 1. Stellar magnitudes and positions are measured with the computer program KS2, which is developed by Jay Anderson and is an evolution of the program kitchen_sync (Anderson et al. 2008).

We used different methods to derive the magnitudes and positions of bright and faint stars. The bright stars have enough flux to derive accurate magnitudes and positions from each individual exposure. Hence, they are measured by fitting the appropriate point-spread function (PSF) model for position and flux in each exposure independently. The best estimates of the magnitude and position of each star correspond to the average of the various measurements. To derive photometry of faint stars, we combined the information from the various exposures. Specifically, we calculated the average position of each star from all exposures, and then we fitted each exposure pixels with the PSF, solving only for the flux. We refer to the paper by Sabbi et al. (2016) for details on the KS2 program.

We used the various diagnostics provided by KS2 to select high-quality stars that are relatively isolated and well fitted by the PSF model as in Milone et al. (2009) and Bedin et al. (2009). We calibrated the photometry into the Vega system as in Bedin et al. (2005) and by using the zero points provided by

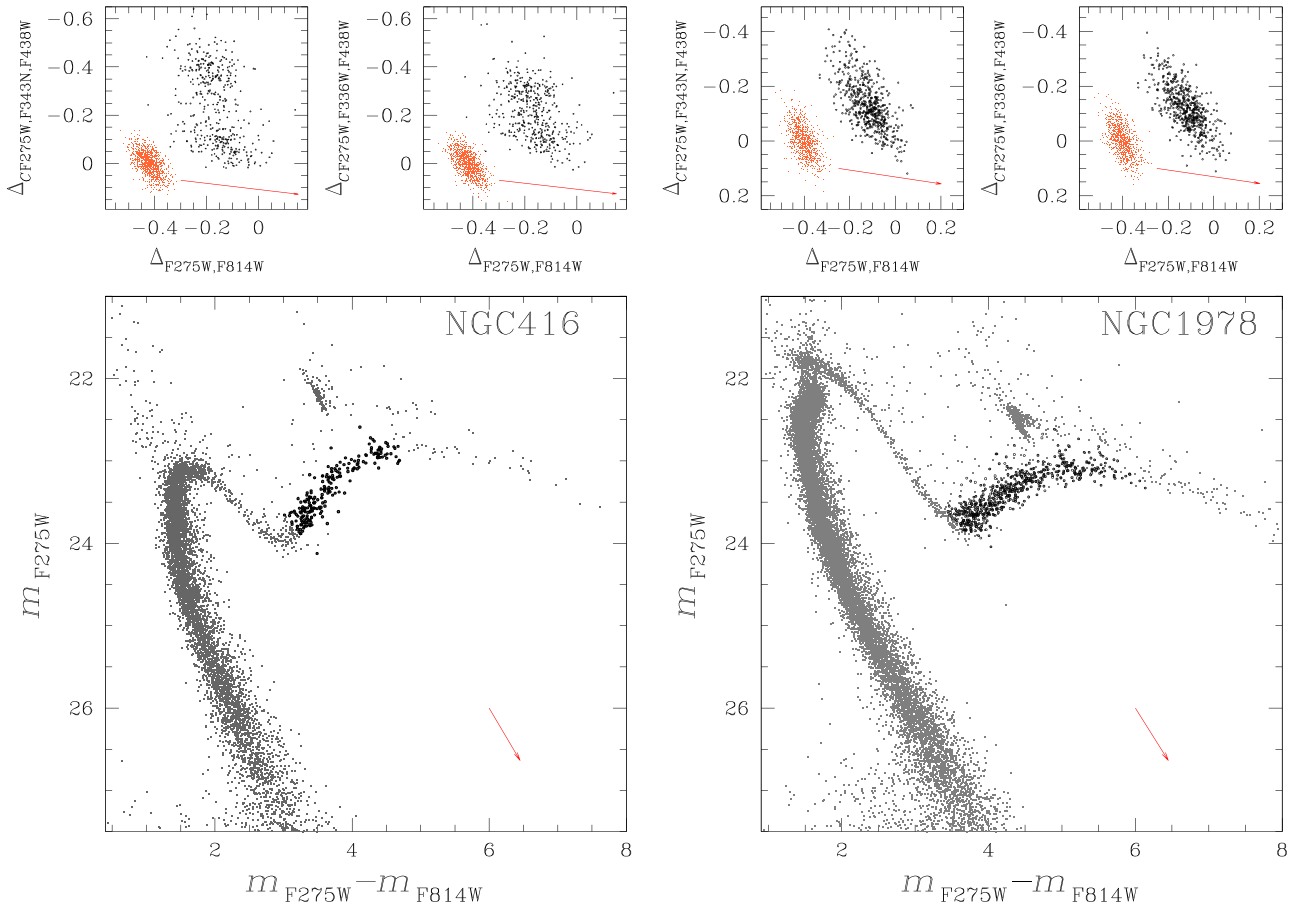

Figure 1. Bottom panels: m_{F275W} vs. $m_{F275W} - m_{F814W}$ CMD of stars in NGC 416 (left) and NGC 1978 (right). Upper panels: $\Delta_{CF275W,F343N,F438W}$ vs. $\Delta_{F275W,F814W}$ and $\Delta_{CF275W,F336W,F438W}$ vs. $\Delta_{F275W,F814W}$ ChMs of RGB stars marked with black dots in the bottom panels. Orange points mark the distribution of observational errors, including errors on differential reddening. Red arrows indicate the reddening vectors and correspond to a reddening variation $\Delta E(B-V) = 0.1$.

the Space Telescope Science Institute webpage.[7] Stellar positions are corrected for geometric distortion by using the solutions provided by Bellini & Bedin (2009) and Bellini et al. (2011).

In addition to HST data, we exploit the astrometric and photometric catalogs of NGC 104, NGC 5927, NGC 6366, and NGC 6838 by Stetson et al. (2019), which provide positions and U, B, V, I magnitudes of stars over wide fields of view (FoVs). Details on the data and the data analysis are provided by Stetson (2005), Stetson et al. (2019), and references therein.

To investigate multiple populations from ground-based photometry, we combined photometry from Stetson et al. (2019) and stellar proper motions from GAIA DR2 (Gaia Collaboration et al. 2018). We selected a sample of cluster members with accurate astrophotometric measurements by using the recipe by Cordoni et al. (2018, 2020). In a nutshell, we first identified stars with accurate proper motions measurements by using both the `astrometric_gof_al` (`As_gof_al`) and the Renormalized Unit Weight Error (RUWE) parameters (Lindegren et al. 2018). We then selected cluster members from the proper motion vector-point diagram (see Cordoni et al. 2018 for details).

Both HST and ground-based photometry have been corrected for the effect of spatial reddening variation by using the method and the computer programs by Milone et al. (2012, see their Section 3.1).

As an example of the photometry derived in this paper, the bottom panels of Figure 1 show the m_{F275W} versus $m_{F275W} - m_{F814W}$ CMD of NGC 416 and NGC 1978 that we used to study multiple populations along both the RGB and the HB. In particular, to characterize stellar populations along the RGB, we derived the $\Delta_{CF275W,F343N,F438W}$ versus $\Delta_{F275W,F814W}$ and $\Delta_{CF275W,F336W,F438W}$ versus $\Delta_{F275W,F814W}$ ChMs of RGB stars plotted in the upper panels of Figure 1. The orange points represent observational errors, including errors on differential reddening, and correspond to the ChMs expected from a simple population (see Milone et al. 2017, 2020a for details). Clearly, the fact that the observed pseudo-color distributions are wider than those expected from observational errors alone corroborates the evidence that NGC 1978 and NGC 416 host multiple stellar populations (Niederhofer et al. 2017; Martocchia et al. 2018b, 2018a; Lagioia et al. 2019a; Milone et al. 2020a).

3. Multiple Populations along the Red HB

As discussed in Section 1, the $m_{F275W} - m_{F336W}$ versus $m_{F336W} - m_{F438W}$ two-color diagram is an efficient tool to identify multiple stellar populations along the MS, subgiant branch (SGB), and RGB of GCs. The reason is that the amount of stellar flux in the F275W, F336W, and F438W bandpasses of HST depends on the strengths of the OH, NH and CN

[7] http://www.stsci.edu/hst/instrumentation/wfc3/calibration and http://www.stsci.edu/hst/acs/analysis/zero-points for WFC3/UVIS and ACS/WFC photometry, respectively.

Table 2
This Table Lists the Average Reddening $E(B-V)$ of Each Cluster and the Random Mean Scatter of Reddening in the Field of View, the Core Radius, the Half-light Radius, the Concentration and Maximum Radial Distance of Our HST Observations

Cluster	$E(B-V)$ (mag)	r.m.s. (mag)	r_c (arcmin)	r_{hl} (arcmin)	c	r_{FoV} (arcmin)
NGC 0104	0.04[a]	0.004[f]	0.36[a]	3.17[a]	2.07[a]	1.66–24.57
NGC 5927	0.45[a]	0.017[f]	0.42[a]	1.10[a]	1.60[a]	0.95–5.96
NGC 6304	0.54[a]	0.012[f]	0.21[a]	1.42[a]	1.80[a]	0.93
NGC 6352	0.22[a]	0.017[f]	0.83[a]	2.05[a]	1.10[a]	0.91
NGC 6366	0.71[a]	0.019[f]	2.17[a]	2.92[a]	0.74[a]	0.90–7.99
NGC 6388	0.37[a]	0.012[f]	0.12[a]	0.52[a]	1.75[a]	1.00
NGC 6441	0.47[a]	0.020[f]	0.13[a]	0.57[a]	1.75[a]	0.92
NGC 6496	0.15[a]	0.014[f]	0.95[a]	1.02[a]	0.70[a]	0.89
NGC 6624	0.28[a]	0.008[f]	0.06[a]	0.82[a]	2.50[a]	0.89
NGC 6637	0.18[a]	0.007[f]	0.33[a]	0.84[a]	1.38[a]	0.94
NGC 6652	0.09[a]	0.005[f]	0.10[a]	0.48[a]	1.80[a]	0.91
NGC 6838	0.25[a]	0.012[f]	0.63[a]	1.67[a]	1.15[a]	0.97–8.94
NGC 1978	0.08[b]	0.003[g]	0.30[c]	0.67[c]	1.26[e]	0.55
NGC 0416	0.05[b]	0.020[g]	0.17[d]	0.25[d]	1.02[h]	0.55

Notes. We also list the maximum radius of the field of view of the ground-based photometry of NGC 104, NGC 5927, NGC 6366, and NGC 6838.
References:
[a] Harris 1996 (2010 edition).
[b] Chantereau et al. (2019).
[c] McLaughlin & van der Marel (2005).
[d] Fischer et al. (1992).
[e] Mateo (1987).
[f] Milone et al. (2012, 2017).
[g] Milone et al. (2020a).
[h] Glatt et al. (2009).

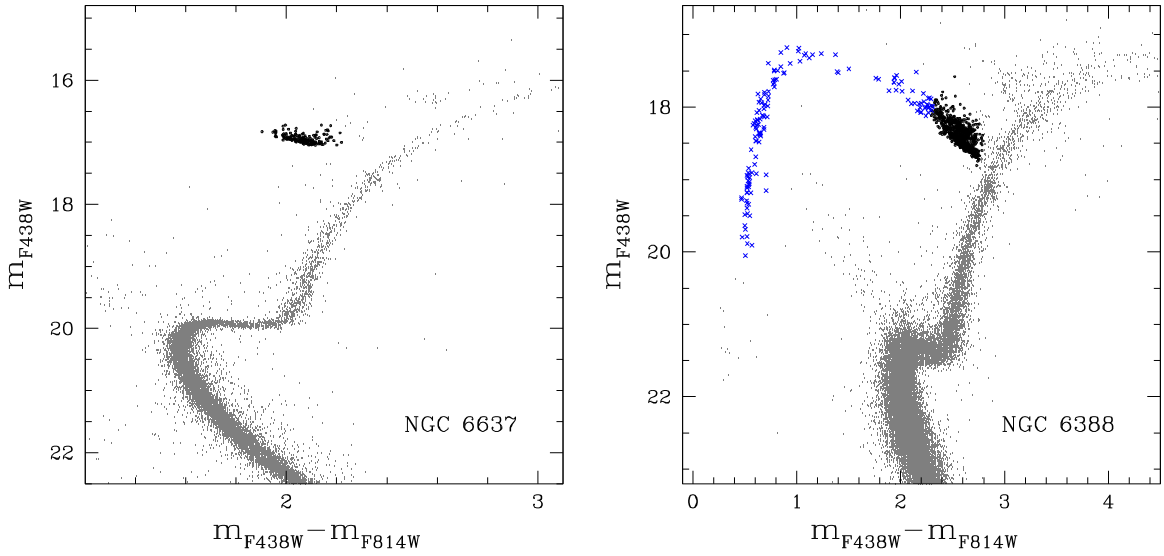

Figure 2. m_{F438W} vs. $m_{F438W}-m_{F814W}$ CMDs corrected for differential reddening of NGC 6388 (left) and NGC 6637 (right). Red HB stars are colored black, while blue HB stars of NGC 6388 are represented with blue crosses.

molecules, which comprise the wavelength range of these filters, and are different for 1G and 2G stars with similar luminosities (e.g., Milone et al. 2012, 2013).

For the same reason, 1G and 2G stars define distinct sequences of red HB stars in the $m_{F275W}-m_{F336W}$ versus $m_{F336W}-m_{F438W}$ plane, and the red HB split is more evident in metal-rich GCs with [Fe/H] $\gtrsim -1.0$. Indeed, similarly to RGB, SGB, and MS stars, the fluxes of their relatively cold red HB stars are strongly affected by the abundances of C, N, and O.

In the following subsection, we exploit photometry in F275W, F336W, and F438W of 12 Galactic GCs with [Fe/H] $\gtrsim -0.8$, namely NGC 104 (47 Tuc), NGC 5927, MGC 6304, NGC 6352, NGC 6366, NGC 6388, NGC 6441, NGC 6496, NGC 6624, NGC 6637, NGC 6652, and NGC 6838 to investigate multiple populations along the red HB. Section 3.3 is dedicated to the LMC GC NGC 1978 and the SMC GC NGC 416.

Table 2 provides relevant quantities for all studied clusters. These comprise the average reddening in the analyzed FoV, $E(B-V)$, the random mean scatter of reddening, the core radius

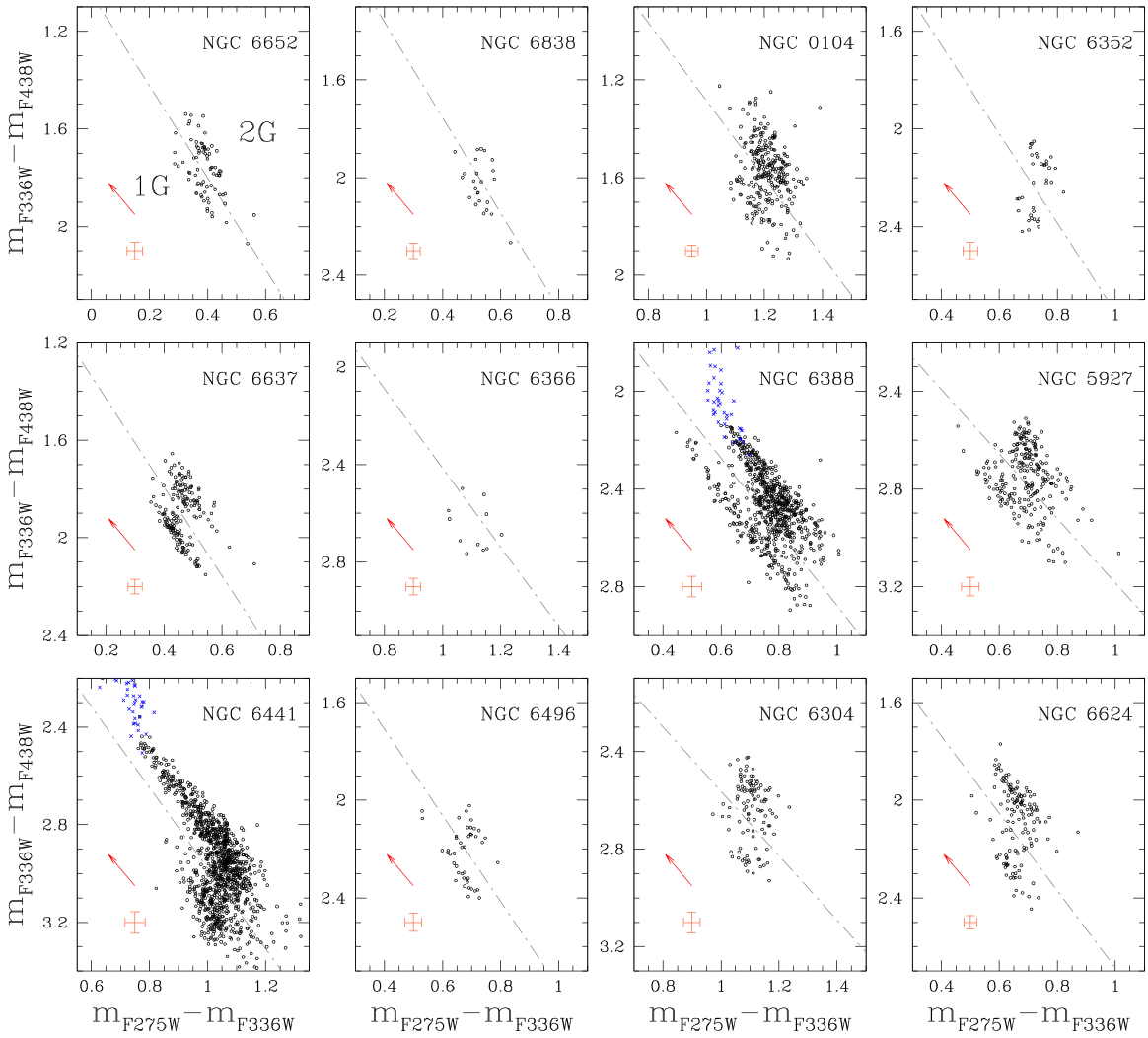

Figure 3. Collection of $m_{F275W} - m_{F336W}$ vs. $m_{F336W} - m_{F438W}$ differential-reddening-corrected two-color diagram diagrams for the red HB stars (black dots) of the studied Galactic GCs sorted by metallicity, from the most metal poor to the most metal rich. Blue HB stars are represented by blue crosses. Gray dotted–dashed lines separate the bulk of 1G stars from 2G. For the sake of comparison, all of the panels span the same interval of $m_{F275W} - m_{F336W}$ and $m_{F336W} - m_{F438W}$. Observational error is represented by orange bars. The reddening vectors corresponding to a reddening variation $\Delta E(B - V) = 0.1$ are represented by red arrows.

(r_c), half-light radius (r_{hl}), and concentration (c). We also indicate the maximum radius covered by HST and ground-based observations, r_{FoV}.

3.1. Disentangling First- and Second-generation Stars along the HB of Galactic GCs

All clusters with [Fe/H] $\gtrsim -0.8$ studied in this paper exhibit the red HB alone. Remarkable exceptions are provided by NGC 6388 and NGC 6441, which also show a blue HB (e.g., Rich et al. 1997). The procedure to identify 1G and 2G stars along the HB of Galactic GCs is illustrated in Figure 2 for NGC 6637, which exhibits the red HB alone, and for NGC 6388, whose HB is populated on both sides of the RR Lyrae instability strip.

We used the differential-reddening-corrected m_{F438W} versus $m_{F438W} - m_{F814W}$ CMDs plotted in Figure 2 to identify by eye the sample of red HB stars that we represented with black dots. Blue HB stars of NGC 6388 are plotted with blue crosses. Once these stars have been selected, they have been plotted in the $m_{F275W} - m_{F336W}$ versus $m_{F336W} - m_{F438W}$ two-color diagrams shown in Figure 3.

Previous work, based on the synergy of photometry, spectroscopy, and theoretical models, has provided empirical evidence that 1G stars populate the red HB sequence with the bluest $m_{F336W} - m_{F438W}$ and reddest $m_{F275W} - m_{F336W}$ colors, while 2G stars exhibit redder $m_{F336W} - m_{F438W}$ and $m_{F275W} - m_{F336W}$ colors than 1G stars (e.g., Milone et al. 2012). As discussed at the beginning of this section, the physical interpretation is straightforward. Indeed, 2G stars are enhanced in nitrogen and depleted in oxygen and carbon with respect to the 1G. Because the F336W filters includes strong NH molecular bands, 2G stars exhibit fainter F336W magnitudes than 1G stars with a similar structure. Similarly, 2G stars have brighter F275W fluxes than the 1G, due to the lower strengths of the OH bands. The F438W band is affected by the CH G band, which makes 2G stars brighter than the 1G, and by the CN band at ~4200 Å, which reduces the F438W flux of 2G stars. The combined effects of these molecular bands can make 2G red HB stars have slightly brighter F438W magnitudes than the 1G. As a consequence, 1G stars have bluer $m_{F336W} - m_{F438W}$ and redder $m_{F275W} - m_{F336W}$ colors than the bulk of 2G stars.

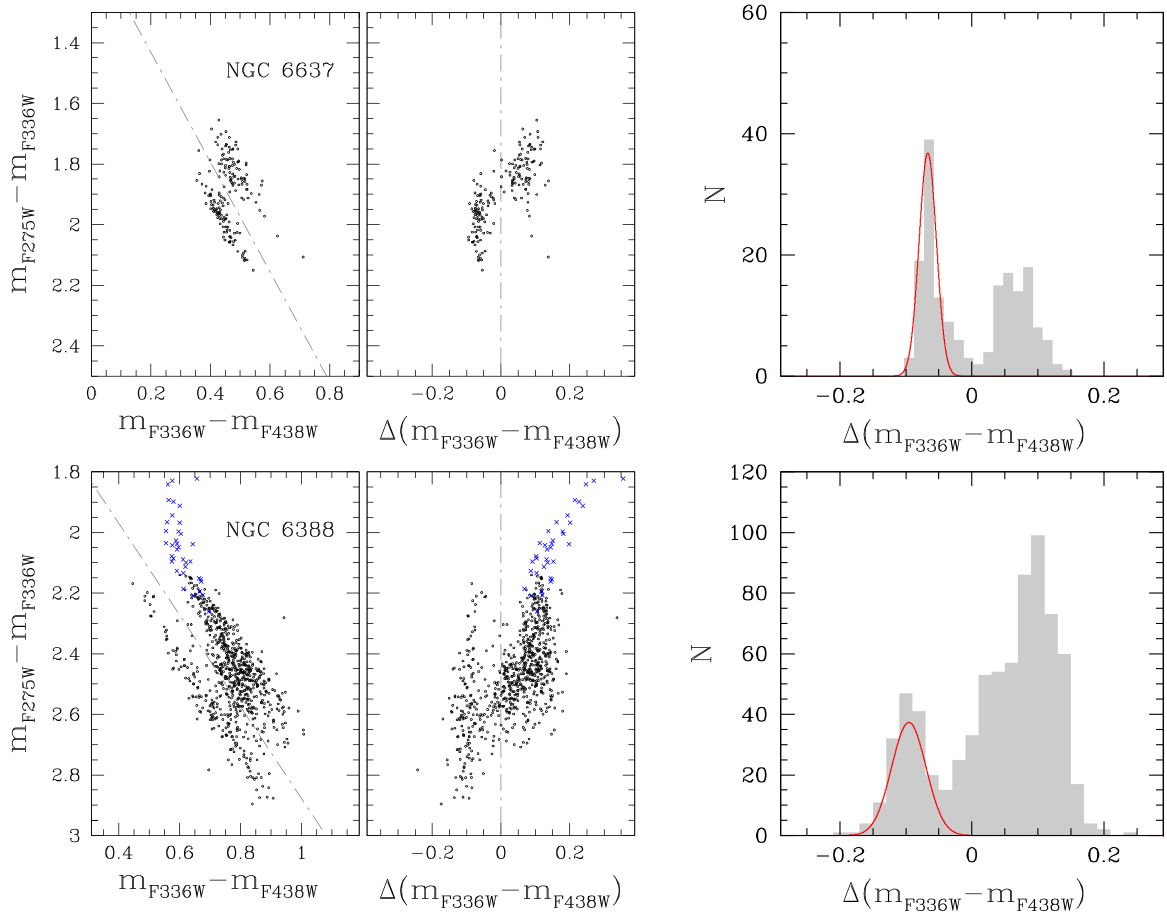

Figure 4. This figure summarizes the main steps to identify 1G stars along the red HBs of NGC 6637 (top panels) and NGC 6388 (bottom panels). The left panels show the $m_{F275W} - m_{F336W}$ vs. $m_{F336W} - m_{F438W}$ two-color diagram of HB stars, blue crosses in the NGC 6388 diagram are the blue HB stars. The gray dashed −dotted lines separate the bulk of 1G stars from the remaining HB stars. The verticalized $m_{F275W} - m_{F336W}$ vs. $\Delta(m_{F336W} - m_{F438W})$ diagrams of HB stars are plotted in the middle panels, whereas the right panels show the $\Delta(m_{F336W} - m_{F438W})$ histogram distributions. The Gaussian function that provides the least-squares best fit with the observed distribution is represented by the red solid line. See text for details.

The dashed gray lines shown in Figure 3 are derived by eye with the criterion of following the fiducial lines of the HB sequence formed by the majority of 2G stars. Driven by the evidence that 1G and 2G stars lie in distinct areas of the two-color diagrams, these lines have been shifted toward bluer $m_{F275W} - m_{F336W}$ colors to separate the majority of 1G stars from the remaining red HB stars.

This collection of diagrams plotted in Figure 3 reveals that all of the Galactic clusters of our sample show multiple populations along the red HB and that the morphology of 1G and 2G stars dramatically changes from one cluster to another. In some clusters, like NGC 6838 and NGC 6352, both 1G and 2G stars span a small interval of less than 0.2 mag in $m_{F275W} - m_{F336W}$, whereas the corresponding color extension of the 1G and 2G sequences of NGC 6388 is wider than ∼0.6 mag. In NGC 6441, the $m_{F275W} - m_{F336W}$ extension of 2G red HB stars is more than two times wider than the 1G color extension.

The number of subpopulations also shows a high degree of variety. NGC 6637 and NGC 6352 exhibit two distinct groups of 1G and 2G stars alone, whereas NGC 6388 and NGC 6441, in addition to the sequences populated by the bulk of 1G and 2G stars, show a subpopulation of 2G stars with intermediate $m_{F336W} - m_{F438W}$ colors.

3.2. The Fraction of First-generation Stars

The procedure to identify the 1G stars and derive their fraction with respect to the total number of HB stars is illustrated in Figure 4 for NGC 6637 and NGC 6388 and is similar to the method introduced by Milone et al. (2012) to infer the fraction of 1G stars along the red HB of 47 Tuc.

The left panels of Figure 4 show the $m_{F275W} - m_{F336W}$ versus $m_{F336W} - m_{F438W}$ two-color diagrams of the cluster HB stars. The gray dashed−dotted lines are used to derive the verticalized $m_{F275W} - m_{F336W}$ versus $\Delta(m_{F336W} - m_{F438W})$ diagrams, which are plotted in the middle panels of Figure 4 and are obtained by subtracting from the $m_{F336W} - m_{F438W}$ color of each star the color of the fiducial line with the same $m_{F275W} - m_{F336W}$.

The histogram distributions of $\Delta(m_{F336W} - m_{F438W})$ are plotted in the right panels of Figure 4 and clearly reveal two main peaks. The bimodal color distribution, which is evident from a visual inspection of Figure 3, is demonstrated by the large values of the bimodality coefficient[8] (BC; SAS Institute

[8] The BC is defined as $BC = \frac{m_3^2 + 1}{m_4 + 3\frac{(n-1)^2}{(n-2)(n-3)}}$, where m_3 and m_4 are the skewness of the distribution and its excess of kurtosis, and n is the number of points of a given distribution, respectively. Bimodal distributions are characterized by values of BC that exceed the critical value $BC_{crit} = 0.555$.

Table 3
Fractions of 1G Stars of GCs Measured in This Paper along the HB and Those Derived in Our Previous Work Based on the RGB (Milone et al. 2017, 2018b; Zennaro et al. 2019; Milone et al. 2020a) and the MS (Milone et al. 2020b)

ID	N_{1G}/N_{TOT} (this work)	$\langle N_{1G}/N_{TOT}\rangle$	r_{FoV}/r_{hl}	ID	N_{1G}/N_{TOT} (this work)	$\langle N_{1G}/N_{TOT}\rangle$	r_{FoV}/r_{hl}
NGC 0104	0.218 ± 0.025	0.180 ± 0.009	0.56	NGC 6397	···	0.345 ± 0.036	0.55
NGC 0288	···	0.558 ± 0.031	0.89	NGC 6441	0.210 ± 0.011	0.210 ± 0.011	2.90
NGC 0362	···	0.279 ± 0.015	2.01	NGC 6496	0.636 ± 0.068	0.666 ± 0.035	1.40
NGC 1261	···	0.359 ± 0.016	2.35	NGC 6535	···	0.536 ± 0.081	1.70
NGC 1851	···	0.264 ± 0.015	3.00	NGC 6541	···	0.396 ± 0.020	1.56
NGC 2298	···	0.370 ± 0.037	1.64	NGC 6584	···	0.451 ± 0.026	2.27
NGC 2419	···	0.370 ± 0.010	2.18	NGC 6624	0.268 ± 0.035	0.276 ± 0.020	1.87
NGC 2808	···	0.232 ± 0.014	2.32	NGC 6637	0.450 ± 0.039	0.426 ± 0.017	2.05
NGC 3201	···	0.436 ± 0.036	0.52	NGC 6652	0.380 ± 0.063	0.349 ± 0.026	3.09
NGC 4590	···	0.381 ± 0.024	1.13	NGC 6656	···	0.274 ± 0.020	0.51
NGC 4833	···	0.362 ± 0.025	0.73	NGC 6681	···	0.234 ± 0.019	2.31
NGC 5024	···	0.328 ± 0.020	1.35	NGC 6715	···	0.267 ± 0.012	2.08
NGC 5053	···	0.544 ± 0.062	0.53	NGC 6717	···	0.637 ± 0.039	2.01
NGC 5139	···	0.086 ± 0.010	0.50	NGC 6723	···	0.363 ± 0.017	1.05
NGC 5272	···	0.305 ± 0.014	0.83	NGC 6752	···	0.294 ± 0.023	0.91
NGC 5286	···	0.342 ± 0.015	2.25	NGC 6779	···	0.469 ± 0.041	1.29
NGC 5466	···	0.467 ± 0.063	0.67	NGC 6809	···	0.311 ± 0.029	0.55
NGC 5897	···	0.547 ± 0.042	0.79	NGC 6838	0.640 ± 0.083	0.630 ± 0.035	0.88
NGC 5904	···	0.235 ± 0.013	0.90	NGC 6934	···	0.326 ± 0.020	2.30
NGC 5927	0.373 ± 0.033	0.373 ± 0.033	1.52	NGC 6981	···	0.542 ± 0.027	1.67
NGC 5986	···	0.246 ± 0.012	1.81	NGC 7078	···	0.399 ± 0.019	1.79
NGC 6093	···	0.351 ± 0.029	2.52	NGC 7089	···	0.224 ± 0.014	1.47
NGC 6101	···	0.654 ± 0.032	1.48	NGC 7099	···	0.380 ± 0.028	1.55
NGC 6121	···	0.290 ± 0.037	0.39	IC 4499	···	0.510 ± 0.050	1.18
NGC 6144	···	0.444 ± 0.037	0.45	Lindsay 1	···	0.663 ± 0.037	0.65
NGC 6171	···	0.397 ± 0.031	0.90	Lindsay 38	···	1.000	1.02
NGC 6205	···	0.184 ± 0.013	1.05	Lindsay 113	···	1.000	···
NGC 6218	···	0.400 ± 0.029	0.93	NGC 0121	···	0.517 ± 0.026	2.12
NGC 6254	···	0.364 ± 0.028	0.86	NGC 0339	···	0.883 ± 0.022	0.64
NGC 6304	0.330 ± 0.046	0.330 ± 0.046	1.13	NGC 0416	0.542 ± 0.044	0.500 ± 0.025	2.20
NGC 6341	···	0.304 ± 0.015	1.63	NGC 0419	···	1.000	1.44
NGC 6352	0.417 ± 0.083	0.497 ± 0.033	0.76	NGC 1783	···	1.000	0.98
NGC 6362	···	0.574 ± 0.035	0.81	NGC 1806	···	1.000	0.14
NGC 6366	0.636 ± 0.182	0.431 ± 0.045	0.51	NGC 1846	···	1.000	1.75
NGC 6388	0.183 ± 0.0120	···	2.45	NGC 1978	0.846 ± 0.029	0.833 ± 0.025	0.82

Note. $\langle N_{1G}/N_{TOT}\rangle$ provides the best estimates of the fractions of 1G stars, derived by combining all results. The last column indicates the ratio between the maximum radius reached by the FoV and the half-light radius. No estimate of the half-light radius of Lindsay 113 is currently available in the literature.

Inc. Staff 1988), which is larger than BC ∼ 0.73 for all studied clusters.

We first selected a raw sample of 1G stars, including all stars with $\Delta(m_{F336W} - m_{F438W})$ values lower than the value corresponding to the minimum of the histogram between the two peaks. We fitted these stars with a Gaussian function by means of least squares, plotted in red in the right panels of Figure 4. The fraction of 1G stars along the HB is derived as the ratio between the area below the red Gaussian and the area of the whole histogram. We verified that the results are not significantly affected by small changes in the slope of the dashed gray lines. To ensure a proper estimate of the fraction of 1G stars in NGC 6388 and NGC 6441, blue HB stars have been included in the total number of 2G stars.

The method described above for NGC 6388 and NGC 6637 has been extended to all Galactic GCs. The resulting fractions of 1G stars are listed in Table 3 and range from ∼15% in NGC 6388 to ∼68% in NGC 6838.

For 9 out of 12 Galactic GCs, namely NGC 104, NGC 6352, NGC 6366, NGC 6388, NGC 6496, NGC 6652, NGC 6624, NGC 6637, and NGC 6838, the fraction of 1G stars along the RGB has been derived by Milone et al. (2017), and in NGC 6352 and NGC 6838, the fraction of 1G stars along the MS was estimated by Milone et al. (2020b), by using the same data set. Our measurements provide the first estimates of population ratios in NGC 5927, NGC 6304, and NGC 6441. For each analyzed cluster, the fraction of 1G stars detected along the red HB is consistent within 1σ with that obtained for the RGB and MS by Milone et al. (2017, 2020b), with the exception of NGC 6388, for which the fraction of 1G stars derived in this work, namely 0.183 ± 0.012, is lower than that inferred by Milone et al. (2017), with a difference significant at the 3σ level. We emphasize that the fractions of 1G stars provided in this section are derived from HST photometry and are representative of the central cluster regions alone. Although the FoV of the majority of studied clusters encloses the half-light radius (see Table 2 of this paper and Table 2 by Milone et al. 2017), the global fraction of 1G stars of some GCs can differ from that observed in the central regions. Indeed, the 2G of some massive GCs is significantly more centrally concentrated than the 1G (e.g., Sollima et al. 2007; Bellini et al. 2009; Milone et al. 2012; Lee 2019; Lee & Sneden 2020).

Figure 5 shows a collection of m_{F438W} versus $m_{F438W} - m_{F814W}$ CMDs for the studied clusters, in which

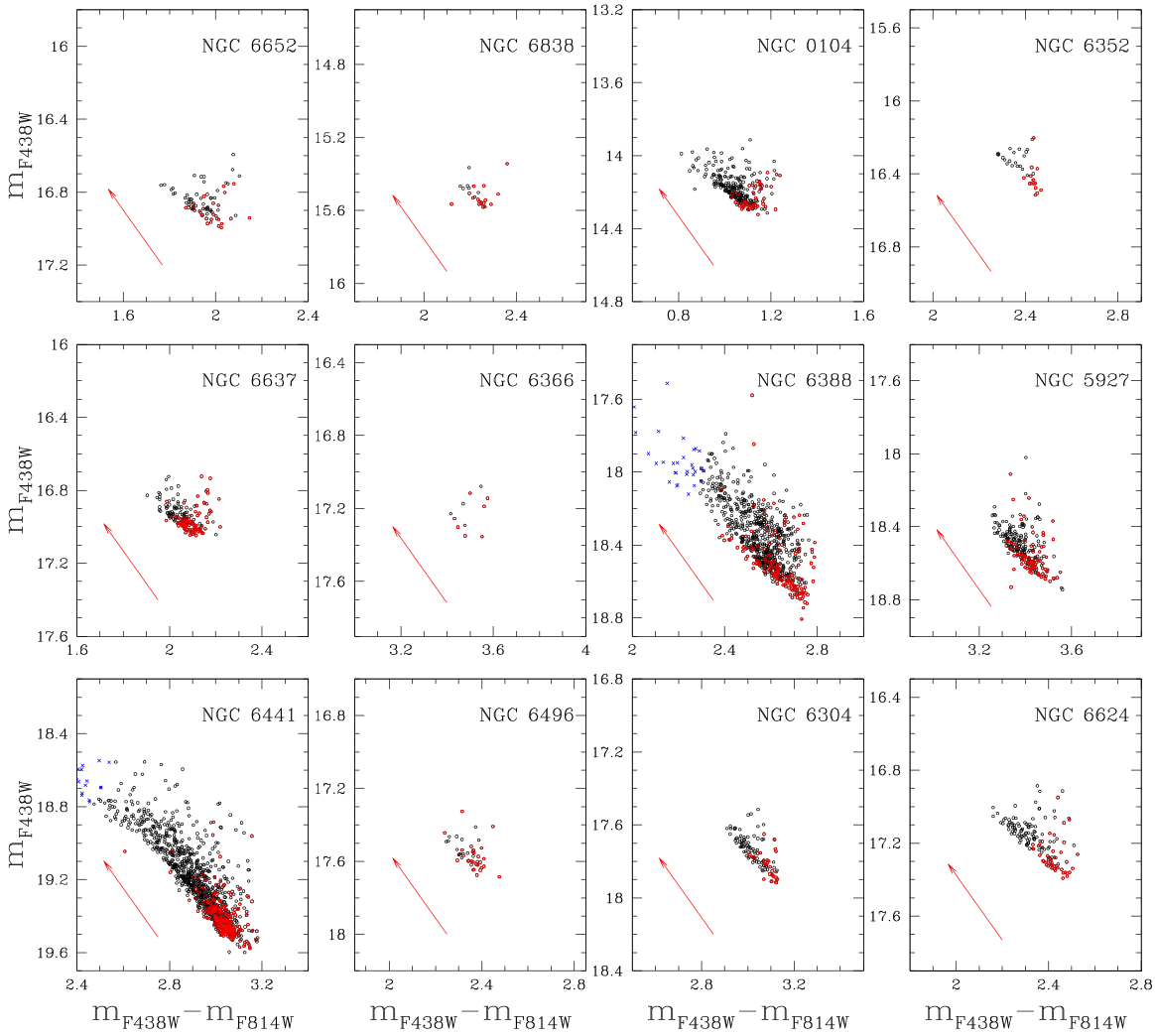

Figure 5. $m_{\rm F438W}$ vs. $m_{\rm F438W} - m_{\rm F814W}$ CMDs for the red HB stars of the Galactic GCs studied in this paper. 1G and 2G stars are colored red and black, respectively. Blue crosses represent the blue HB stars.

we plotted in red the selected 1G stars. Colors made with optical magnitudes are strongly affected by $T_{\rm eff}$ variations and hence are sensitive to stellar populations with different helium abundances. Optical magnitudes have low sensitivity to light-element abundance variations when compared with ultraviolet bands, although the F438W and F814W filters are significantly affected by carbon and nitrogen variations. As expected, the sample of 1G stars exhibit, on average, redder $m_{\rm F438W} - m_{\rm F814W}$ colors and fainter $m_{\rm F438W}$ magnitudes than the bulk of 2G stars. This fact is consistent with the previous findings that 2G stars are typically enhanced in helium and depleted in carbon with respect to the 1G (see, e.g., Lagioia et al. 2018; Milone et al. 2018b; Tailo et al. 2020 for determinations of the chemical composition of 1G and 2G stars along the RGB and the HB).

3.3. Multiple Populations in Magellanic Cloud Clusters

In this section, we exploit multiband photometry of the Galactic GC 47 Tuc, where multiple populations along the HB have been extensively studied, to introduce new two-color diagrams that allow 1G and 2G stars along the red HB to be disentangled. These diagrams will then be used as tools to identify for the first time 1G and 2G stars along the red HB of the SMC cluster NGC 416 and the red clump of the LMC cluster NGC 1978.

Indeed, in addition to F275W, F336W, and F438W data, images in F343N are available for 47 Tuc, NGC 1978, and NGC 416. The F343N, which is a narrow filter that comprises the spectral region that includes various NH and molecular bands, is mostly sensitive to stellar populations with different nitrogen abundances. Hence, we exploited this filter to build the two-color $(m_{\rm F275W} - m_{\rm F343N})$ versus $(m_{\rm F343N} - m_{\rm F438W})$ diagram and the $C_{\rm F336W,F343N,F438W} = (m_{\rm F336W} - m_{\rm F343N}) - (m_{\rm F343N} - m_{\rm F438W})$ versus $m_{F438W} - m_{F814W}$ pseudo-two-color diagram for red HB and red clump stars. Results are illustrated in the upper panels of Figure 6 for 47 Tuc, where we compare the classic $(m_{\rm F275W} - m_{\rm F336W})$ versus $(m_{\rm F336W} - m_{\rm F438W})$ two-color diagram with the diagrams introduced in this work. Clearly, the fact that the bulk of selected 1G and 2G stars (red and black points in Figure 6) populate distinct regions in each diagram demonstrates that the two-color and pseudo-two-color diagrams that involve photometry in F343N are powerful tools to

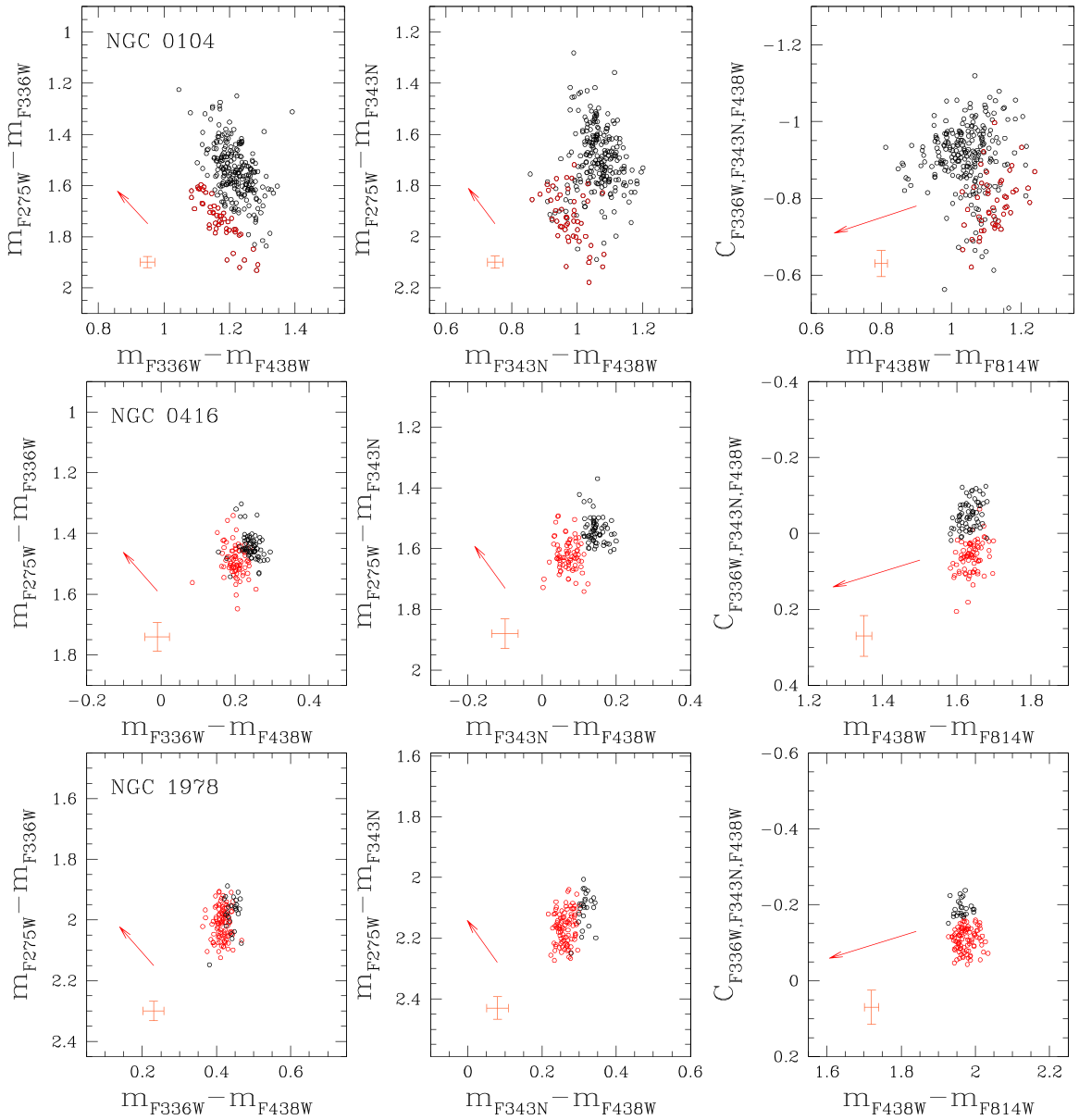

Figure 6. ($m_{F275W} - m_{F336W}$) vs. ($m_{F336W} - m_{F438W}$) (left panels), ($m_{F275W} - m_{F343N}$) vs. ($m_{F343N} - m_{F438W}$) (central panels), and $C_{F336W,F343N,F438W}$ vs. $m_{F438W} - m_{F814W}$ (right panels) two-color diagrams for 47 Tuc (top), NGC 416 (middle), and NGC 1978 (bottom). Selected 1G and 2G stars are colored red and black, respectively. Red arrows indicate the reddening vectors for $\Delta E(B - V) = 0.1$.

detect multiple populations along the red HB and the red clump.[9]

These diagrams are plotted in the middle and lower panels of Figure 6 for NGC 416 and NGC 1978, respectively, and reveal that both clusters host multiple populations along the red HB and the red clump. By using the method described in Section 3.2, we find that in contrast with what is observed in the majority of Galactic GCs, which are dominated by the 2G (Milone et al. 2017), the majority of red HB and red clump stars in both NGC 416 and NGC 1978 belong to the first generation (54.2% ± 4.4% and 84.6% ± 2.9%). Figure 7 shows the optical CMDs of NGC 416 and NGC 1978, in which red and black points indicate, respectively, 1G and 2G stars. While 2G stars are significantly brighter and bluer than the 1G in the optical CMDs of Galactic GCs (Figure 5), stars of both populations of NGC 416 and NGC 1978 are distributed along the whole red HB and red clump.

3.4. Comparison with Simulated Multiple Populations

The behavior of simple-population stars along the red clump and HB phases is well constrained from theory. In a nutshell, when a low-mass RGB star reaches the RGB tip, the temperature in its core becomes sufficiently high ($\sim 10^8$ K) to allow helium ignition, starting at the HB phase, during which stars burn helium via 3α reaction, producing carbon and oxygen. At the start of helium burning, the core mass is almost the same for all stars ($\sim 0.45\ M_\odot$). Because the luminosity in this phase depends mainly on the core mass, stars in the HB have approximately the same luminosity, so they are arranged

[9] We remind readers that the groups red HB stars marked with red and blue colors include the majority of 1G and 2G stars, respectively, and that some contamination is expected. Such small contamination is negligible for our purpose of showing that 1G and 2G stars populate distinct regions in the diagrams of Figure 6.

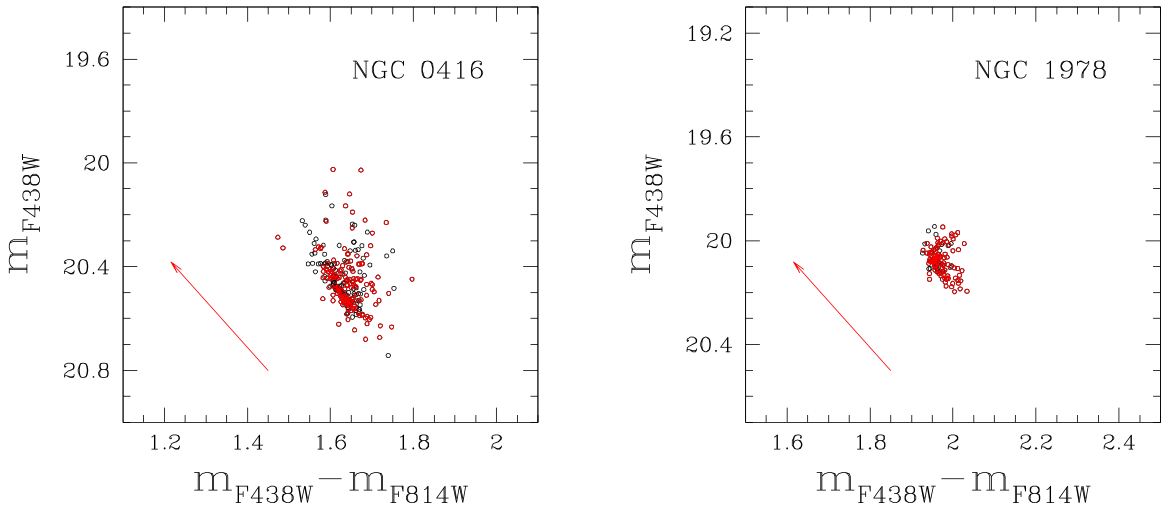

Figure 7. Comparison of the NGC 416 red HB (left panel) and the NGC 1978 red clump (right panel) in optical CMDs. 1G stars are colored in red.

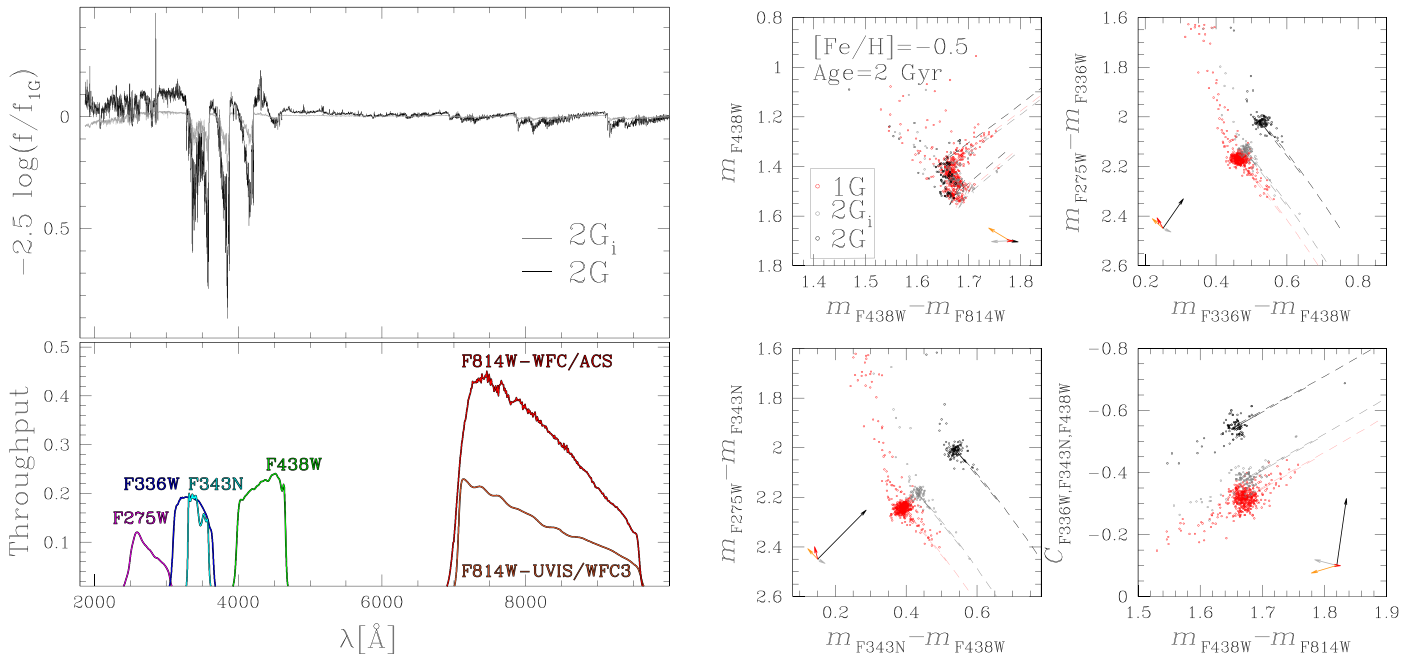

Figure 8. Left panels: flux ratio between the spectrum of 2G (black) or $2G_i$ star (gray) and the spectrum of 1G star with T_{eff} = 4,898 K and log g = 2.46 (upper panel). The throughputs of the filters used in this paper are plotted in the bottom panel. Right panels: simulated diagrams of 2 Gyr old HB stars with the same iron abundance, [Fe/H] = −0.5. Red and black dots correspond to 1G and 2G stars, respectively, while gray dots have similar chemical composition to 2G stars of NGC 1978, which are enhanced in nitrogen by 0.1 dex with respect to the 1G. The corresponding isochrones are represented by dashed lines. The gray, black, red, and orange vectors indicate the effect of changing C, N, O, and Fe, respectively, one at time, on the colors and magnitudes. See text for details.

along a horizontal sequence in CMDs. During this evolutionary phase, the envelope mass can vary from star to star (e.g., Iben & Rood 1970; Dorman 1992). Stars with lower initial mass or that have experienced a larger amount of mass loss during the RGB phase have smaller envelope masses, hence different colors. Indeed, the effective temperature (T_{eff}) depends on the envelope mass: lower envelope masses lead to lower T_{eff}, therefore to redder stars. In the case of multiple-population GCs, the position of a star along the red HB or the red clump may also depend on its chemical composition (e.g., D'Antona et al. 2002; Salaris et al. 2008).

To further investigate the impact of light-element abundance variations on the colors and magnitudes of red HB and red clump stars, we qualitatively compared the observed photometric diagrams with simulations. To do this, we first extended to the red clump the method used in a previous work from our group, which is based on synthetic spectra with different chemical compositions (see e.g., Milone et al. 2012, 2018b for details). We first simulated the colors and magnitudes of red clump stars in a stellar population with age 2.0 Gyr and [Fe/H] = −0.5, based on MESA isochrones (Paxton et al. 2011, 2013, 2015; Choi et al. 2016; Dotter 2016). To do this, we identified six points along the isochrone and extracted their effective temperatures and gravities. For each point, we computed a reference spectrum with solar-scaled light-element abundances that mimics 1G stars and two comparison spectra that correspond to 2G stars with different chemical compositions. Specifically, we simulated a spectrum of a 2G star enhanced in nitrogen by 0.6 dex and depleted in both C and O by 0.3 dex, and a spectrum of a stellar population (hereafter

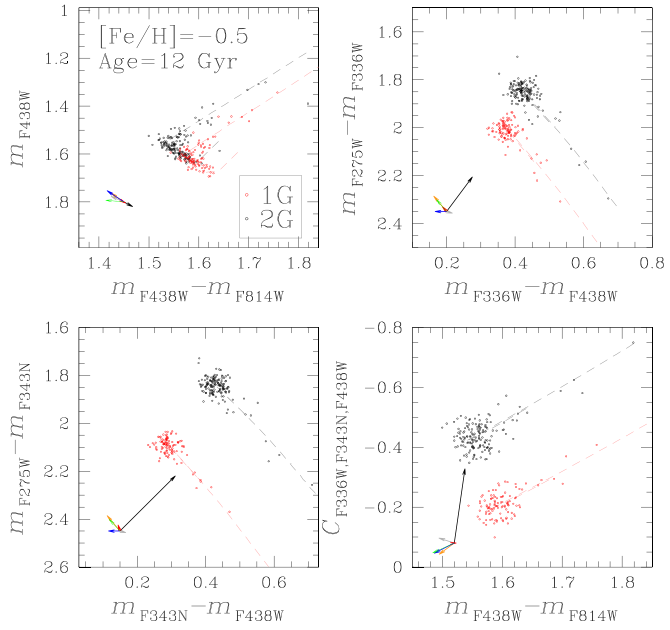

Figure 9. Simulated diagrams of 12 Gyr old stellar populations with [Fe/H] = −0.5. The blue, gray, black, red, orange, and green vectors indicate the effect of changing He, C, N, O, Fe, and mass loss, respectively, one at time, on the colors and magnitudes. See text for details.

against the fluxes of a 2G star and a $2G_i$ star with $T_{eff} = 4{,}898$ K and log $g = 2.46$, relative to the 1G star with the same atmosphere parameters. For completeness, we show the throughputs of the F275W, F336W, F343N, F438W, and F814W UVIS/WFC3 filters and the F814W ACS/WFC filter used in this paper.

Stellar magnitudes are calculated by integrating synthetic spectra over the bandpasses of the filters used in this paper and are used to derive the magnitude difference, δm_X, between the comparison and reference spectrum. Hence, we derived the magnitudes of simulated 2G and $2G_i$ stars by adding to the 1G isochrones the corresponding values of δm_X.

The isochrones of 2G and $2G_i$ stars are finally used to derive the simulated diagrams illustrated in the right panels of Figure 8, where we adopted the mass function by Salpeter (1955) and assumed that 35% of the sources in the CMD are binary systems, which is the typical binary fraction inferred in intermediate-age Magellanic Cloud star clusters (Milone et al. 2009). We added to simulated photometry the typical uncertainties of our observations as inferred from NGC 1978 by using artificial-star tests (see, e.g., Anderson et al. 2008 for details).

We find that 2G and $2G_i$ stars are almost indistinguishable from the 1G in the m_{F438W} versus $m_{F438W} - m_{F814W}$ CMD and have higher $m_{F336W} - m_{F438W}$ and $m_{F343N} - m_{F438W}$ colors

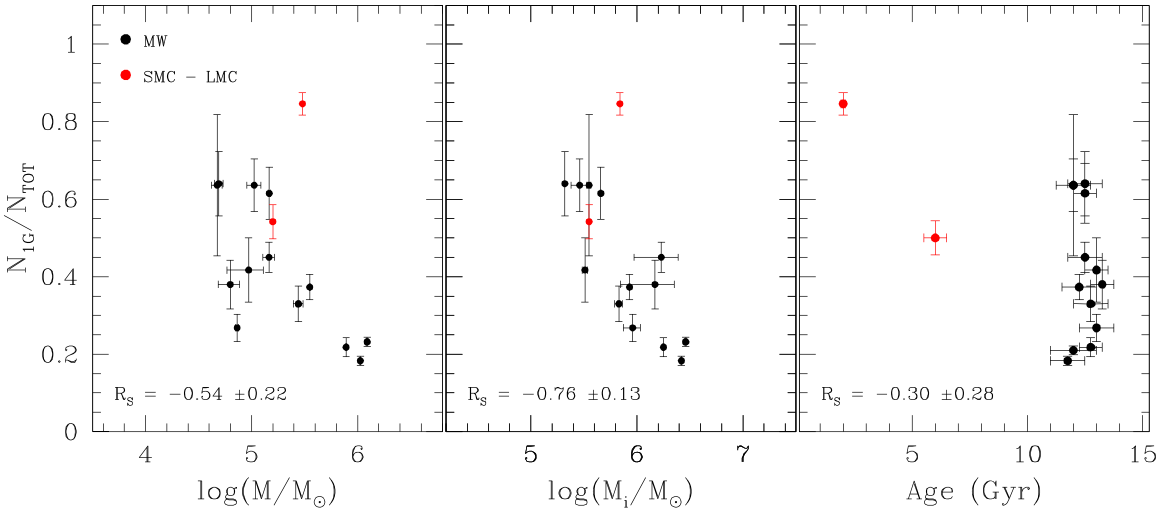

Figure 10. The fractions of 1G stars calculated in this work from the HB are plotted against the present-day mass (left) and the initial mass (middle) and cluster ages. Galactic GCs are shown in black, while red dots indicate the extragalactic clusters.

$2G_i$) with [C/Fe] = 0.0, [N/Fe] = +0.1, and [O/Fe] = 0.0 as inferred by Milone et al. (2020a) for NGC 1978. We assumed a microturbulent velocity of 2 km s^{-1} for all stars, which is higher than the values inferred for red HB stars (e.g., Afşar et al. 2018). We verified that adopting microturbulent velocity of 2 km s^{-1} has a negligible impact on the relative colors of 1G and 2G stars and does not change our conclusions, thus confirming the previous conclusion by Sbordone et al. (2011). Atmosphere models are computed by using the computer program ATLAS12 (Kurucz 1970, 1993; Sbordone et al. 2004), which is based on the opacity-sampling method and assumes local thermodynamic equilibrium. We derived synthetic spectra in the wavelength interval between 1800 and 10000 Å by using SYNTHE (Kurucz & Avrett 1981; Castelli 2005; Kurucz 2005; Sbordone et al. 2007). As an example, in the upper-left panel of Figure 8, we plot the wavelength

than the 1G. Moreover, 2G and $2G_i$ stars exhibit lower values of $m_{F275W} - m_{F336W}$, $m_{F275W} - m_{F343N}$, and $C_{F336W,F343N,F438W}$ than the 1G. Although a quantitative comparison between the observed and the simulated diagrams is beyond the purposes of our work, we note that the observed behavior of the selected stellar populations of NGC 1978 qualitatively matches the simulated 1G and $2G_i$. This fact further demonstrates that the red clump of NGC 1978 is not consistent with a simple isochrone but hosts two stellar populations with different chemical compositions.

The color differences between the simulated stellar populations are mostly due to the NH molecular bands that affect the F336W and F343N filters. Because 2G and $2G_i$ stars are enhanced in nitrogen with respect to the 1G, they exhibit fainter magnitudes in the F336W and F343N than 1G stars with the same atmosphere parameters. Moreover, 2G stars are O poor

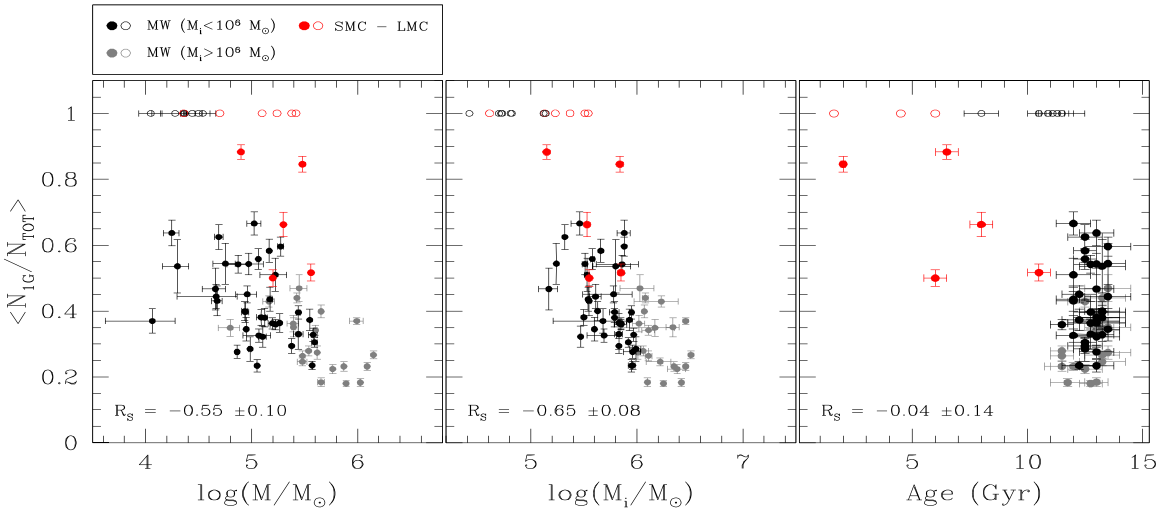

Figure 11. Weighted mean of the fraction of 1G stars vs. the present-day mass (left) initial mass (middle) and the age of the host GC (right). Black and gray dots represent, respectively, Galactic GCs with $M_i < 10^6\ M_\odot$ and $M_i < 10^6\ M_\odot$, and red dots represent extragalactic GCs. The cluster without MPs are represented with open circles.

and C poor. Hence, they exhibit brighter F275W and F438W magnitudes as a consequence of the strengths of the OH and CN molecules that affect the F275W and F438W fluxes, respectively. For completeness, we investigate the effect of C, N, O, and Fe abundance variations on the diagrams Figure 8. The gray, black, red, and orange vectors plotted on the bottom-left corner of each panel show the average effect of changing [C/Fe], [N/Fe], [O/Fe], and [Fe/H] by −0.3, +0.6, −0.3, and −0.1 dex, respectively.

We also extended the analysis to 12 Gyr old HB stars with [Fe/H] = −0.5. In this case, we exploited α-enhanced isochrones from the Roma database (e.g., Tailo et al. 2019a and references therein). We assumed that 1G stars have solar-scaled carbon and nitrogen abundances and [O/Fe] = 0.4, while 2G stars are enhanced in N by 0.6 dex and depleted in both C and O by 0.3 dex, with respect to the 1G. We adopted helium content Y = 0.25 for 1G stars and assumed that the 2G is enhanced by 1% in helium mass fraction, which is the typical helium difference between 2G and 1G stars in GCs (e.g., Lagioia et al. 2018; Milone et al. 2018b). We adopted a fraction of binaries of 0.10, which is consistent with results based on MS stars of GCs (e.g., Milone et al. 2016).

Results are illustrated in Figure 9 and are qualitatively consistent with observations of Galactic GCs. Specifically, 2G stars exhibit bluer $m_{\rm F438W} - m_{\rm F814W}$ colors than the 1G. In this case, the color difference is mostly due to the hotter temperature of He-rich 2G HB stars. Similarly to what was observed in the simulated red clumps, 2G stars have higher $m_{\rm F336W} - m_{\rm F438W}$ and $m_{\rm F343N} - m_{\rm F438W}$ colors and lower values of $m_{\rm F275W} - m_{\rm F336W}$, $m_{\rm F275W} - m_{\rm F343N}$, and $C_{\rm F336W,F343N,F438W}$ than the 1G. These color differences are mostly due to C, N, and O variations that impact the flux in the F275W, F336W, F343N, and F438W bands mostly through CN, CH, OH, and NH molecules. The gray, black, red and orange vectors plotted on the bottom-left corner of each panel of Figure 9 illustrate the effect of changing [C/Fe], [N/Fe], [O/Fe], and [Fe/H], one at time, by −0.3, +0.6, −0.3, and −0.1 dex, respectively. Blue and green arrows correspond to the helium mass fraction and an RGB mass loss increase of ΔY = 0.03 and $\Delta\ \mathcal{M} = 0.02\ \mathcal{M}_\odot$, respectively.

4. Relations with the Parameters of the Host Globular Clusters

In the following, we analyze the relation between the observed fraction of 1G stars and cluster mass, which represents the GC parameter that shows the strongest correlation with several MP indicators (e.g., Milone et al. 2020a), and with cluster age that is possibly associated with the MP phenomenon (e.g., Martocchia et al. 2018b). In the left and middle panels of Figure 10, we show that the fractions of 1G stars derived from the red HBs and the red clumps anticorrelate with both present-day mass, M, and the initial masses $M_{\rm i}$ of the host GCs (from Glatt et al. 2011; Goudfrooij et al. 2014; Baumgardt & Hilker 2018; Baumgardt et al. 2019; Milone et al. 2020a).[10] This fact is indicated by the Spearman's rank correlation coefficients, which are $R_{\rm s} = -0.54 \pm 0.22$ and $R_{\rm s} = -0.76 \pm 0.13$, respectively. We do not find a significant correlation with cluster ages (from Milone et al. 2009; Dotter et al. 2010; Lagioia et al. 2019b; Milone et al. 2014, $R_{\rm s} = -0.30 \pm 0.28$) as illustrated in the right panel of Figure 10.

To increase the number of GCs, we exploited results from this paper and from previous work based on RGB and MS stars from our group (Milone et al. 2017, 2018b; Tailo et al. 2019b; Zennaro et al. 2019; Milone et al. 2020a). The fractions of 1G stars derived in the literature are consistent with those in our paper at the 1σ level for all GCs, with the exception of NGC 6388, which is consistent at the $\sim$3σ level only.

We improved the determination of the fraction of 1G stars by calculating $\langle N_{\rm 1G}/N_{\rm TOT}\rangle$, which is the weighted mean of the various estimates of $N_{\rm 1G}/N_{\rm TOT}$, when available. Results are listed in Table 3. In Figure 11, the same diagrams of Figure 10 are shown for this larger sample of clusters. Based on a large sample of GCs with multiple populations, we find correlations with present-day and initial masses ($R_{\rm s} = -0.55 \pm 0.10$ and

[10] The values used in this paper are the state of the art for $M_{\rm i}$ of GCs. Nevertheless, these values are affected by various uncertainties, associated with our poor knowledge of the Galaxy the Magellanic Clouds and their tidal fields (see Section 2.2 by Milone et al. 2020a). In addition, significant uncertainties may come from poorly known processes that occurred during the formation and early evolution of star clusters and of their MPs whose impacts are not taken into account in calculating $M_{\rm i}$ (e.g., Renzini et al. 2015).

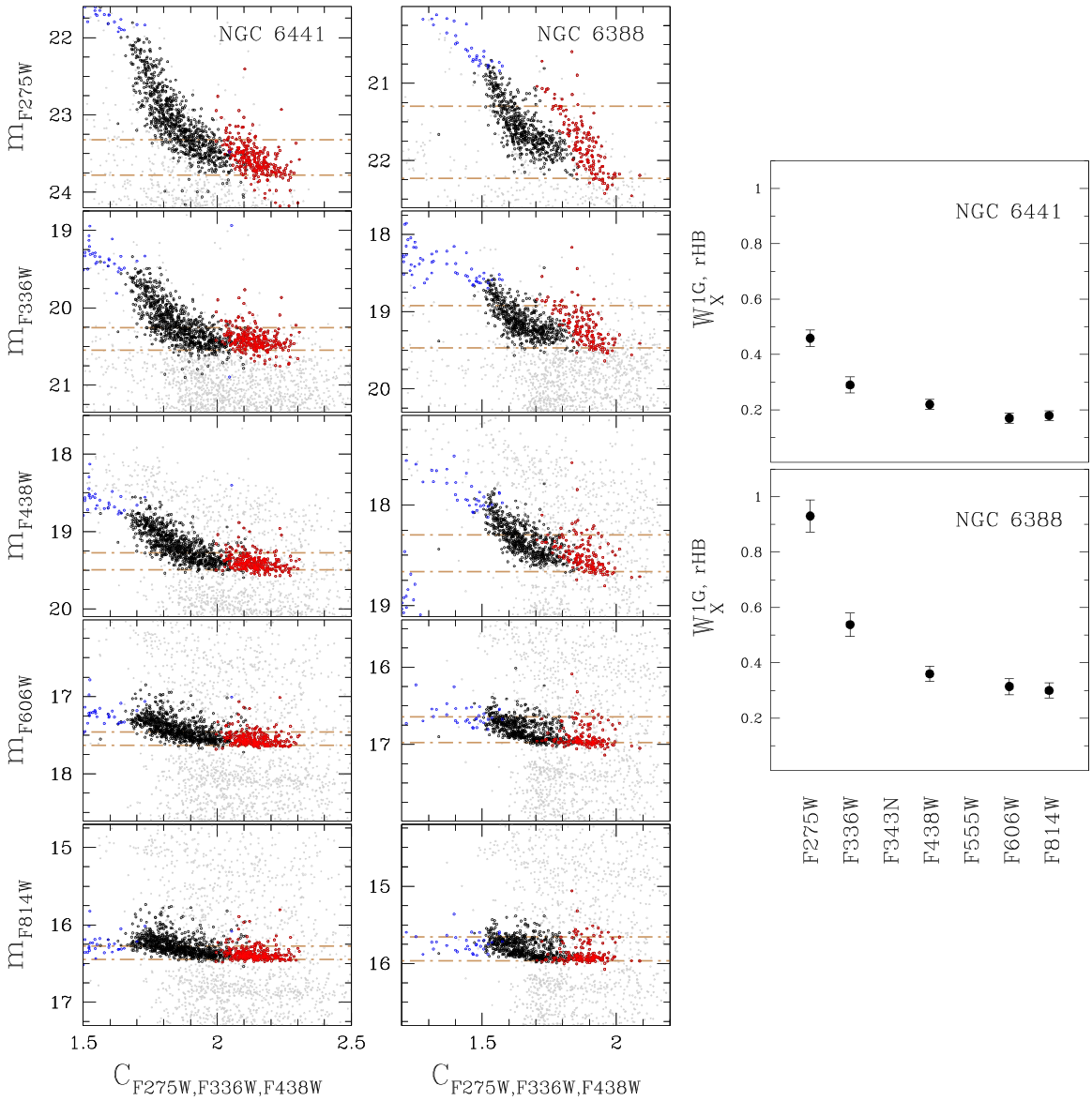

Figure 12. Comparison between the red HBs of NGC 6441 (left panels) and NGC 6388 (middle panels) in the m_X vs. $C_{F275W,F336W,F438W}$ planes, where X = F275W, F336W, F438W, F606W, and F814W. 1G stars, 2G red HB, and 2G blue HB stars are colored red, black, and blue, respectively, while the remaining cluster stars are represented with gray points. The two brown horizontal dotted–dashed lines mark the 10th and 90th percentiles for the magnitude distribution of 1G stars. Right panels show the magnitude extension of 1G stars, $W_X^{1G,rHB}$, for the available filters.

$R_s = -0.65 \pm 0.08$, respectively). Such correlations are confirmed when we extend the analysis to clusters without multiple populations (open symbols in Figure 11), which provides higher values of $R_s = -0.65 \pm 0.08$ and $R_s = -0.80 \pm 0.05$ for the anticorrelations with present-day and initial masses, respectively.

When we consider GCs with multiple populations alone, we find no evidence of a correlation between the fraction of 1G stars and cluster age ($R_s = -0.04 \pm 0.14$), and we get the same conclusion when we consider only clusters with initial masses smaller than $10^6 M_\odot$ (black and red filled dots in Figure 11). On the contrary, the analysis of all GCs, including the simple population of star clusters, provides a significant anticorrelation between the fraction of 1G stars and the cluster ages ($R_s = -0.60 \pm 0.07$). This result reflects the evidence that all analyzed GCs older than ∼12 Gyr host multiple populations, while all studied clusters younger than ∼2 Gyr are consistent with simple populations.

5. The Color and Magnitude Extensions of 1G Stars

Figure 3 reveals that the color and magnitude extensions of 1G stars significantly change from one cluster to another.

NGC 6388 and NGC 6441, which are traditionally considered twin clusters, are remarkable examples.[11] Indeed, NGC 6388 shows a very extended 1G sequence in the two-color diagrams of Figure 3, while 1G stars of the HB of NGC 6441 span relatively small $m_{F275W} - m_{F336W}$ and $m_{F336W} - m_{F438W}$ color intervals.

To further compare the red HBs of NGC 6388 and NGC 6441, we plot in the left and middle panels of Figure 12 the

[11] NGC 6388 and NGC 6441 share very similar masses, metallicities ([Fe/H] ∼ −0.50), and they are both located in the Galactic bulge. The existence of bHB stars in these clusters was an unexpected feature given their relatively high metallicity (e.g., Rich et al. 1997) and was considered one of the earliest signatures of stellar populations with extreme helium abundances in GCs (e.g., D'Antona & Caloi 2008; Tailo et al. 2017 and references therein).

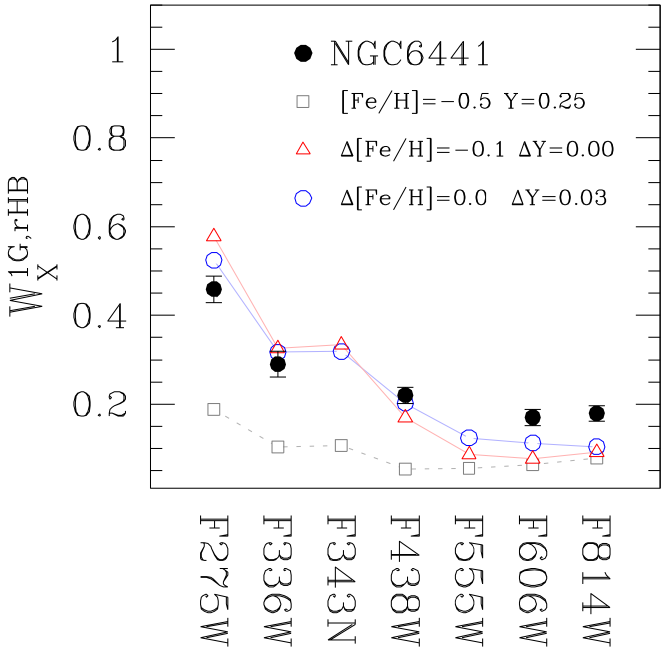

Figure 13. Comparison between the observed magnitude extension of 1G stars along the red HB of NGC 6441 (black circles) and simulated HBs with different helium contents and metallicities. Gray squares correspond to a simple stellar population with [Fe/H] = −0.5 and pristine helium abundance ($Y = 0.25$), red triangles represent a stellar system composed of two stellar populations with pristine helium content and [Fe/H] = −0.5 and [Fe/H] = −0.6, whereas blue circles correspond to a stellar system composed of two stellar populations with the same [Fe/H] and helium abundances $Y = 0.25$ and $Y = 0.28$.

$C_{F275W,F336W,F438W}$ versus m_X diagram of their HB stars, where X = F275W, F336W, F438W, F606W and F814W. In each panel, the two brown horizontal dotted–dashed lines indicate the 10th (upper) and the 90th (lower) percentiles of the magnitude distribution. The vertical distance observed between the two lines $W^{1G,rHB}_X$, has been plotted in the right panels of the figure as a function of the filter. From this figure, we see that the red HB magnitude extension of NGC 6388 is slightly larger than that of NGC 6441 (∼0.3 versus ∼0.2 mag), but the difference suddenly diverges as we move to blue and UV wavelengths. The most pronounced difference is in the F275W band, where the value of $W^{1G,rHB}_{F275W}$ measured for NGC 6388 is ∼0.45 mag larger than that of NGC 6441.

The 1G of NGC 6441 is further investigated in Figure 13, where we compare the observed values of $W^{1G,rHB}_X$ with those derived from simulated HBs that account for observational errors and correspond to a simple population with pristine helium abundance, age of 12.0 Gyr, and [Fe/H] = −0.5, suitable for NGC 6441 (Harris 1996; Dotter et al. 2010). Clearly, the observed red HB of 1G stars of NGC 6441 spans wider magnitude ranges than the simulated HB (gray squares in Figure 13), thus demonstrating that the 1G of this cluster is composed of stars with different chemical compositions.

Recent work, based on MS and RGB stars, revealed that 1G stars of most studied clusters exhibit extended sequences in the ChM (Milone et al. 2015, 2017). The analysis of 1G stars through multiband photometry shows that the extended sequence is consistent with either star-to-star variations of helium abundance (e.g., Milone et al. 2015, 2018b) or with intrinsic metallicity spread (e.g., D'Antona et al. 2016; Tailo et al. 2019a). The latter hypothesis is supported by direct spectroscopic measurements of iron abundances of NGC 3201 (Marino et al. 2019b).

To investigate the physical reasons that are responsible for the 1G extension of HB stars in NGC 6441, we simulated the red HB of a stellar system composed of two stellar populations with pristine helium content and iron abundances [Fe/H] = −0.5 and −0.6, so with an iron variation of Δ[Fe/H] = −0.1, and derived the corresponding values of $W^{1G,rHB}_X$ (red triangles in Figure 13). Moreover, we simulated the red HB of a stellar system hosting two stellar populations with [Fe/H] = −0.5 and different helium abundances of $Y = 0.25$ and $Y = 0.28$ (blue circles in Figure 13).

The simulated HBs are derived from the stellar models by (Tailo et al. 2016; M. Tailo et al. 2020, in preparation). We determined the mass of the each HB star as $M^{HB} = M^{Tip} - \Delta M(\mu, \delta)$, where M^{Tip} is the mass at the RGB tip derived from the best-fit isochrone and ΔM is the mass lost by the star, during the RGB. Specifically, we adopted a Gaussian profile for ΔM, with average mass loss of 0.25 $M_\odot$ and mass-loss dispersion of $0.006 M_\odot$, which is the average value inferred by Tailo et al. (2020) for the studied GCs.

Figure 13 reveals that the observed HB magnitude extensions of 1G stars in NGC 6441 are consistent with two stellar populations with [Fe/H] = −0.5 that differ in helium mass fraction by $\Delta Y \sim 0.03$. As an alternative, observations are well reproduced by stellar populations with the same helium content, $Y = 0.26$, but different iron abundances at a level of ∼0.1 dex ([Fe/H] = −0.5 and [Fe/H] = −0.6). Hence, similarly to what was observed on the ChM (Milone et al. 2017), from our data set, it is not possible to disentangle between internal helium and metallicity variations as responsible for the magnitude extension of 1G HB stars in NGC 6441. A similar conclusion can be extended to the other studied GCs.

Because we verified that at the typical luminosities of the red HB stars, both NGC 6388 and NGC 6441 show comparable magnitude errors in each band, we infer from the observation that in Figure 12, the spread of the NGC 6388 1G red HB stars is larger than that of NGC 6441 in all five bands, and that also the 1G population of NGC 6388 is not consistent with being a simple stellar population.

Figure 14 shows the magnitude extensions of the 1G red HB and red clump stars in different filters for all studied GCs. Similarly to what is observed in NGC 6388 and NGC 6441, the $W^{1G,rHB}_X$ quantities values approach their maximum for X = F275W in all clusters but NGC 1978, which exhibits a nearly constant magnitude extension in all filters. The F336W extension is significantly wider than that measured in optical bands in NGC 416, NGC 5927, NGC 6388, and NGC 6441, whereas the other clusters share similar magnitude extension in F336W and optical bands. In NGC 6637 and NGC 6652, the F336W and F438W magnitude extensions are slightly narrower than those in F606W and F814W.

To investigate the relation between the color extension of the sequence formed by 1G stars along the red HB and the RGB, we exploit the red HB width $W^{1G,rHB}_{F336W,F438W}$, derived as the difference between the 90th and the 10th percentiles of the red HB 1G stars' $m_{F336W} - m_{F438W}$ color distribution, listed in Table 4. Figure 15 shows that $W^{1G,rHB}_{F336W,F438W}$ correlates with the width of the ChM of 1G stars $W^{1G,RGB}_{F275W,F814W}$, which is the difference between the 90th and the 10th percentiles of the RGB 1G stars $\Delta_{F275W,F814W}$ distribution (from Milone et al. 2017), and with the present-day mass of the host GC (from

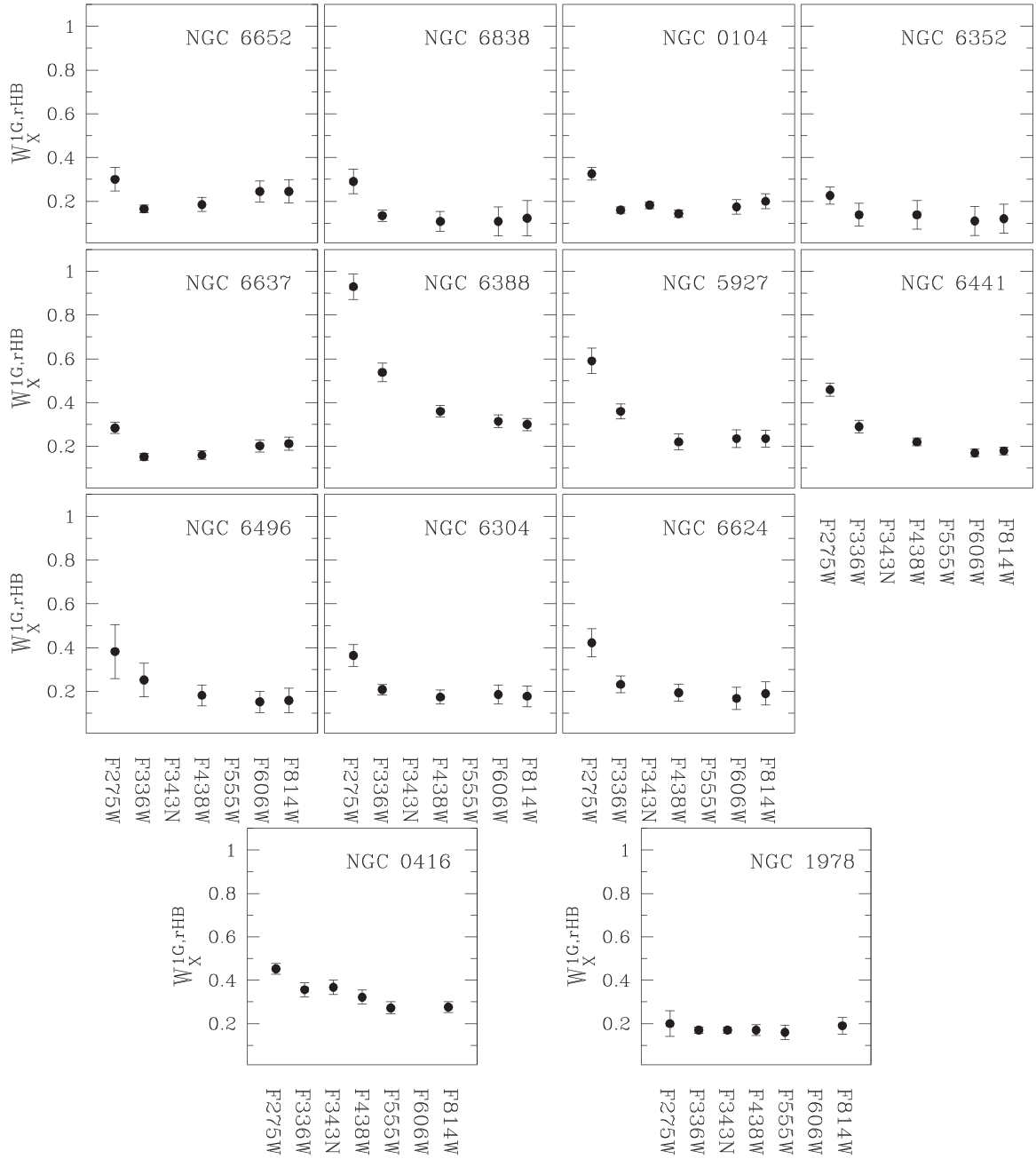

Figure 14. Width of 1G stars along the red HB in the X magnitude, $W_X^{1G,rHB}$ for Galactic and extragalactic GCs, as a function of the various filters used in this work.

Baumgardt & Hilker 2018). There is no evidence of a relation between the color extension of 1G HB stars and the age of the host GCs (from Dotter et al. 2010).

For completeness, we extended the analysis to the whole HB and derived the corresponding color widths $W^{rHB}_{F336W,F438W}$ that are listed in Table 4. As shown in Figure 16, $W^{rHB}_{F336W,F438W}$ correlates with both the RGB width and the cluster mass. No significant correlations has been found with age, in close analogy with what is observed for the color extension of 1G HB stars.

6. Radial Distribution of Multiple Populations

To investigate the radial distributions of multiple populations in 47 Tuc, NGC 5927, NGC 6366, and NGC 6838, we combined information from the HST observations that cover a central region of $\sim 2\farcm7 \times 2\farcm7$, with ground-based photometry catalogs by Stetson et al. (2019), which are extended over a wider FoV.

Indeed, previous work has shown that the photometric diagrams including U and B photometry are efficient tools to identify 1G and 2G stars from ground-based photometry (e.g., Marino et al. 2008; Milone et al. 2012; Monelli et al. 2013).

To further demonstrate that the sequences of red HB stars observed in the $m_{F275W} - m_{F336W}$ versus $m_{F336W} - m_{F438W}$ and V versus $C_{U,B,I}$ diagrams correspond to the 1G and 2G stars, we exploit both observations and simulated photometry. The upper panels of Figure 17 compare these two diagrams for NGC 6838 and use red and black colors to represent 1G and 2G stars, respectively, with both ground-based and HST photometry. Clearly, the groups of 1G and 2G stars selected from the

Table 4
Extension of the F336W − F438W Color of 1G Red HB Stars and All Red HB Stars of the Galactic and Extragalactic Clusters of Our Sample

Cluster	$W^{1G,rHB}_{F336W,F438W}$	$W^{rHB}_{F336W,F438W}$
NGC 0104	0.120 ± 0.018	0.138 ± 0.009
NGC 5927	0.200 ± 0.018	0.180 ± 0.013
NGC 6304	0.123 ± 0.020	0.100 ± 0.012
NGC 6352	0.060 ± 0.008	0.095 ± 0.016
NGC 6388	0.250 ± 0.018	0.210 ± 0.008
NGC 6441	0.140 ± 0.012	0.200 ± 0.008
NGC 6496	0.095 ± 0.034	0.107 ± 0.023
NGC 6624	0.102 ± 0.021	0.120 ± 0.011
NGC 6637	0.104 ± 0.014	0.110 ± 0.006
NGC 6652	0.125 ± 0.028	0.100 ± 0.014
NGC 6838	0.090 ± 0.028	0.094 ± 0.023
NGC 1978	0.050 ± 0.006	0.051 ± 0.007
NGC 0416	0.060 ± 0.007	0.080 ± 0.006

two-color diagram populate distinct sequences in the V versus $C_{U,B,I}$ pseudo-CMD, and a similar conclusion can be derived for the other analyzed GCs with available HST and ground-based photometry.

This result is corroborated by the simulations of 1G and 2G stars introduced in Section 3.4 for 12 Gyr old stellar populations with [Fe/H] = −0.5. As shown in the bottom panels of Figure 17, simulated 1G and 2G stars populate distinct regions of the $m_{F275W} - m_{F336W}$ versus $m_{F336W} - m_{F438W}$ and V versus $C_{U,B,I}$ planes.

The procedure to estimate the fraction of 1G and 2G stars along the red HB from ground-based photometry is summarized in the upper-left panels of Figure 18 for 47 Tuc. The V versus $C_{U,B,I}$ diagram of this cluster exhibits a split HB as noticed in previous work (Monelli et al. 2013; Milone et al. 2018a; Cordoni et al. 2020). The $C_{U,B,I}$ histogram distribution of HB stars is fitted by a bi-Gaussian function by means of least squares. The Gaussian components corresponding to the 1G and the 2G are colored red and blue, respectively, and the relative numbers of 1G and 2G stars are derived by comparing the area below the red and blue Gaussians.

We find that the fraction of 2G stars of 47 Tuc derived from ground-based photometry between 1.′5 and 24.′0 is 0.67 ± 0.02, and it is significantly smaller than that observed within ∼1′ from the cluster center, 0.78 ± 0.03. Similarly, the fraction of 2G stars of NGC 5927 in the region with radial distance between ∼0.′5 and 6.′0 from the cluster center, 0.58 ± 0.03, is smaller than that derived from HST photometry (0.63 ± 0.03). These results are consistent with clusters where the 2G is more centrally concentrated than the 1G. On the contrary, the fraction of 2G stars of NGC 6366 and NGC 6838, measured within 8.′0 and 9.′0 from the center, are consistent with the corresponding values inferred from HST photometry in the central field.

To further investigate the dependence of the relative numbers of 1G and 2G stars from the radial distance, we divided the FoV of ground-based photometry into different radial bins, each containing almost the same number of HB stars. We estimated the fractions of 1G and 2G stars in each radial bin by using the procedure described in Figure 18.

Results are illustrated in Figure 19, where we plot the fraction of 2G stars as a function of the radial distance from the cluster center. The dashed and dotted–dashed gray lines correspond, respectively, to the values of the core radius and the half-,light radius (from Harris 1996, 2010 edition, for Galactic GCs; from McLaughlin & van der Marel 2005 for NGC 416; and from Fischer et al. 1992 for NGC 1978). In 47 Tuc the fraction of 2G stars is maximum near the cluster center and is consistent with a flat distribution within ∼0.7 half-light radii. The fraction of 2G stars drops from ∼0.8 to ∼0.65 at about 1.0 half-light radius, and then, it slightly decreases to ∼0.55 at larger radial distances. Similarly, the fraction of 2G stars of NGC 5927 is close to ∼0.7 within ∼1.5 half-light radii and decreases to ∼0.4 in the region around three half-light radii.

On the contrary, in NGC 6366 and NGC 6838, there is no evidence for a radial gradient. Noticeably, the fractions of 2G stars in the internal regions inferred in this paper from the HB are in agreement with those derived from RGB and MS stars by Milone et al. (2017, 2020b).

The radial distributions of multiple populations in GCs with no available ground-based photometry have been derived by

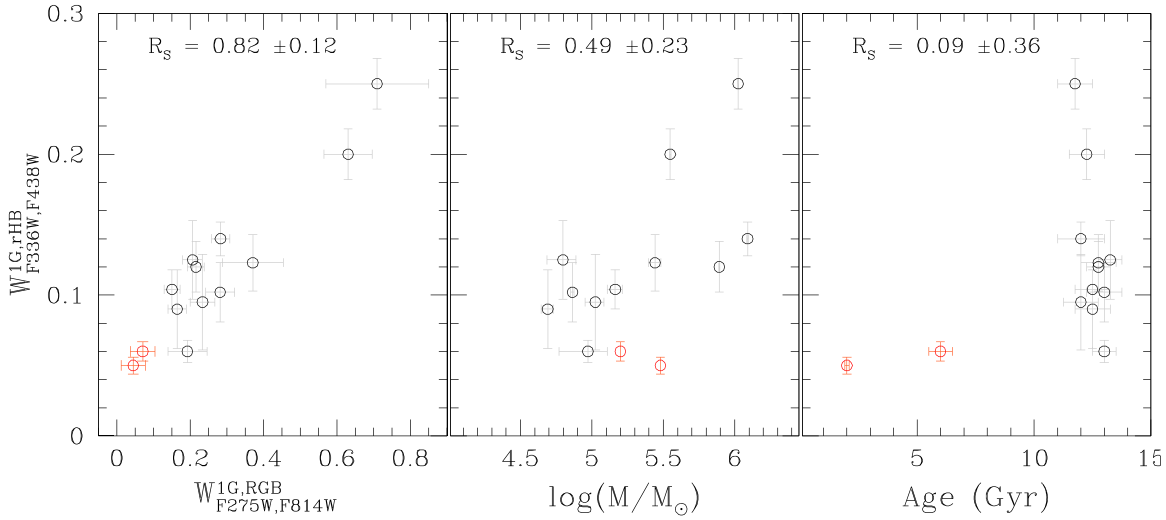

Figure 15. $m_{F336W} - m_{F438W}$ color extension of 1G stars along the HB against the width of 1G RGB stars along the ChM $W^{1G,RGB}_{F275W,F814W}$ (from Milone et al. 2017, left panel), the mass of the host GC (from Baumgardt & Hilker 2018, middle panel) and GC ages (from Dotter et al. 2010, right panel). The Spearman rank correlation coefficients are quoted on top of each panel.

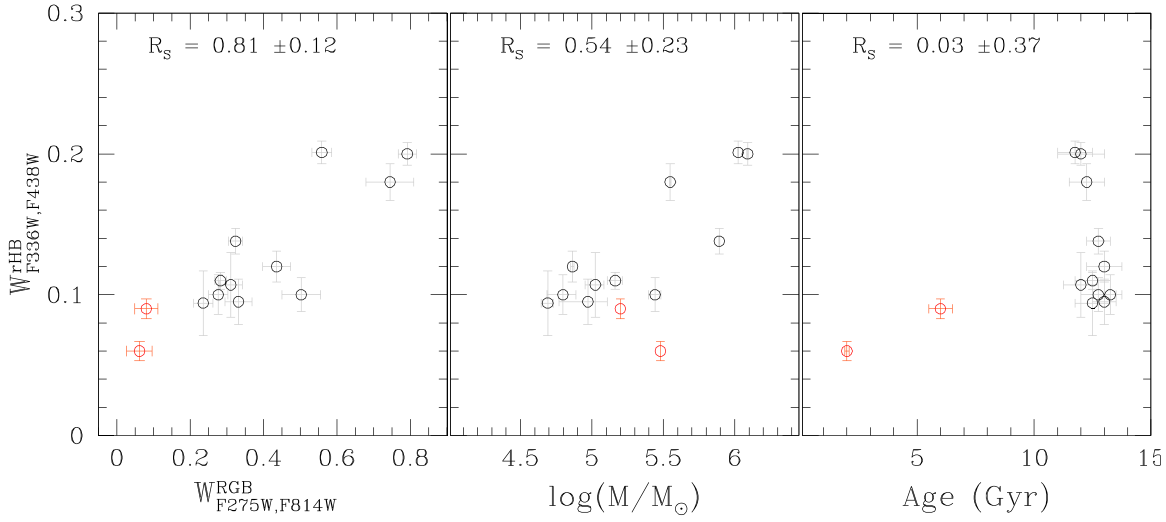

Figure 16. Same as Figure 15, but for the $m_{\rm F336W} - m_{\rm F438W}$ color extension of stars along the whole red HB.

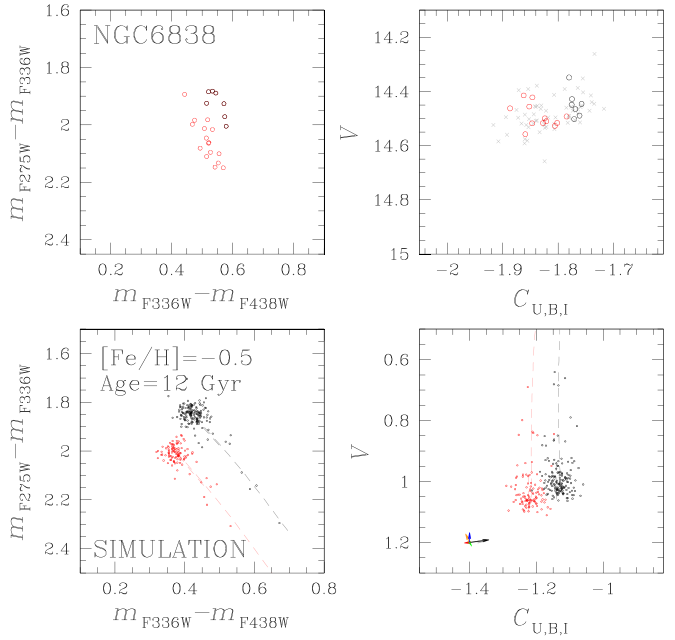

Figure 17. Comparison between $m_{\rm F275W} - m_{\rm F336W}$ vs. $m_{\rm F336W} - m_{\rm F438W}$ (left) and V vs. $C_{\rm U,B,I}$ (right) diagrams for red HB stars. Upper panels show the observed diagrams of NGC 6838 from HST and ground-based photometry. 1G and 2G stars, selected from the left panel two-color diagram are plotted in red and black, respectively, in both panels. Lower panels illustrate results for simulated diagrams. The vectors plotted in the lower-right panel are defined as in Figure 9.

using HST photometry alone. Hence, the investigation is limited to the innermost $\sim 1'$ from the cluster center. We divided the HST FoV of each cluster in various radial intervals comprising similar numbers of HB stars and derived the fraction of 1G and 2G stars by following the procedure of Section 3.2.

Results are illustrated in Figure 20. We find that the majority of Galactic clusters are consistent with a flat radial distribution of 2G stars in the innermost arcmin. NGC 416 is a possible exception. Indeed, its 2G stars seem to be more centrally concentrated than the 1G.

The statistical significance of the observed 1G and 2G radial distributions has been estimated by running 10,000 simulations with a flat radial distribution of stars, under the null hypothesis that the observed distribution profiles are produced by statistical fluctuations. For each simulation, the radial distribution has been obtained starting from the the observed $N_{\rm 2G}/N_{\rm TOT}$ weighted-average ratios across the covered radial distance and then adding up a random radial scatter based on the observed errors. By using a chi-square test, we measured the deviation from flatness, represented by the quantity $\chi^2_{\rm sim}$. We finally compared this value with $\chi^2_{\rm obs}$ and determined the number of times for which $\chi^2_{\rm sim} > \chi^2_{\rm obs}$. This number, divided by the total number of simulations, gives an estimate of the p value, which is the probability that the chi-square is equal to or higher than the one measured. The p value corresponding to $X^2_{\rm obs}$ value of each cluster is reported in Table 5. We see that $p \leqslant 0.05$ only for 3 out of 14 GCs (47 Tuc, NGC 5927, and NGC 416), which means in turn that the observed scatter can be truly associated with a different population radial distribution.

Our results corroborate previous evidence that the 2G of 47 Tuc is more centrally concentrated than the 1G (e.g., Milone et al. 2012; Cordero et al. 2014).

Dalessandro et al. (2018) investigated the radial distribution of multiple populations in 20 GCs and quantified the radial difference between 1G and 2G stars by using the area enclosed between their cumulative radial distributions, A^+, within two half-light radii from the center. The sample of GCs studied by Dalessandro et al. (2018) comprises three GCs, namely NGC 1978, NGC 6624, and NGC 6637, also studied in this paper.

Although it is not possible to quantitatively compare our results with those by Dalessandro and collaborators, due to the different methods adopted, we notice that NGC 6624 and NGC 6637 exhibit values of A^+ that are close to zero, thus indicating that 1G and 2G stars exhibit similar radial distributions to those found in this paper. On the contrary, results on NGC 1978 from Dalessandro et al. (2018) are in disagreement with our conclusion of mixed 1G and 2G stars in this cluster. Indeed, the large and negative value of $A^+ = -0.081$ indicates that its 2G is significantly more centrally concentrated than the 1G.

The comparison between our results on NGC 6441 and those by Bellini et al. (2013) is even more puzzling. Based on the $m_{\rm F390W}$ versus $m_{\rm F390W} - m_{\rm F606W}$ CMD, Bellini and

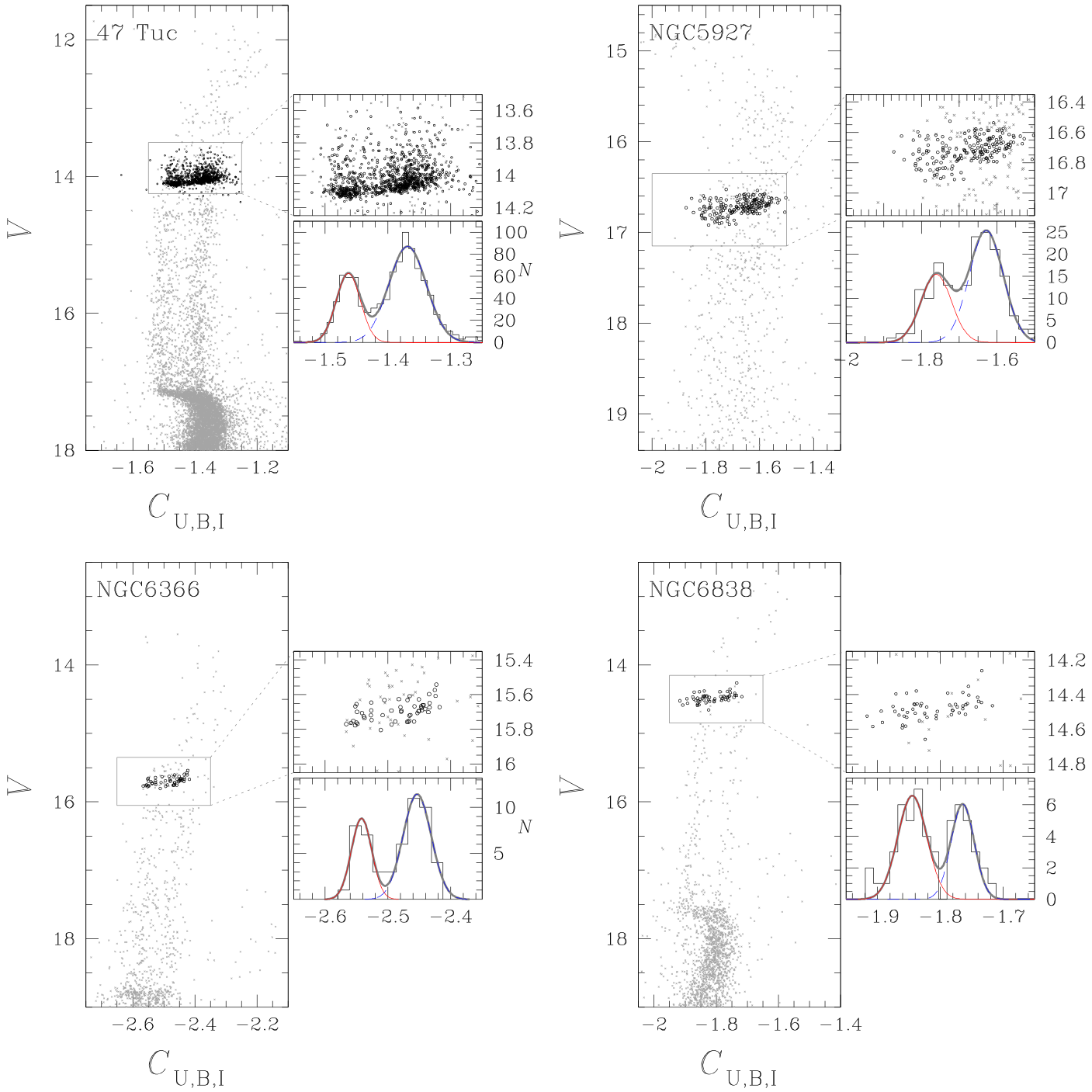

Figure 18. V vs. $C_{U,B,I}$ pseudo-two-color diagrams of selected cluster members of 47 Tuc, NGC 5927, NGC 6366, and NGC 6838 from ground-based photometry (Stetson et al. 2019). Red HB stars are marked by black dots, while the remaining stars are plotted in gray dots. A zoom of the CMD region around the HB is provided in the small panels on the right together with the histogram distributions of $C_{U,B,I}$ for red HB stars. The red and blue curves superimposed on the histogram represent the Gaussian functions that provide the best fit of the two peaks.

collaborators identified split MS and RGB in NGC 6441. Both the blue MS and the blue RGB are more centrally concentrated than their red counterparts. Specifically, the fraction of blue MS stars ranges from ∼0.4 for radial distance from the cluster center, $R \sim 0\farcm9$, to ∼0.35 at $R \sim 2\farcm5$. The fraction of blue RGB stars varies from ∼0.6, near the cluster center, to ∼0.5 at $R \sim 2\farcm5$. Clearly, the fractions of blue RGB and blue MS stars are smaller than the fraction of 2G stars derived in this paper, thus indicating that the blue sequences identified by Bellini and collaborators encloses only part of the 2G of NGC 6441. This fact, together with the larger radial interval covered by the observations analyzed by Bellini et al. (2013), is likely the reason for the different conclusions from these two papers.

7. Summary and Conclusions

In this work, we exploited the red HB to investigate the phenomenon of multiple stellar populations in 14 GCs, based on the distribution of red HB stars in UV-optical two-color diagrams. This allowed us to identify and characterize, for the

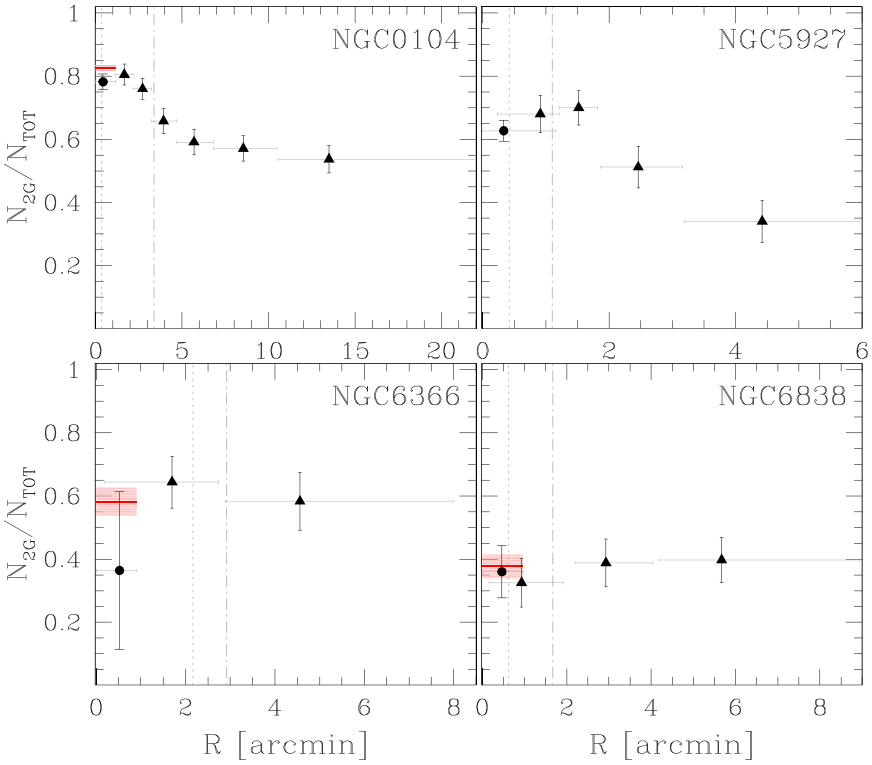

Figure 19. Fraction of 2G stars as a function of radial distance for 47 Tuc, NGC 5927, NGC 6366, and NGC 6838. Black circles and triangles mark the results derived from HST and ground-based photometry, respectively. Gray horizontal lines mark the extension of each radial interval, while the red segments indicate results from Milone et al. (2017, 2020a) based on RGB stars. The vertical dotted and dashed–dotted lines indicate the core and the half-light radius.

first time, the MPs along the red HB in a large sample of ∼13 Gyr old Galactic GCs and in the extragalactic GCs NGC 416 and NGC 1978, which have ages of ∼2 and ∼6 Gyr, respectively.

To do this, we exploited multiband photometry obtained from images collected with the ACS/WFC and WFC3/UVIS cameras on board HST. In particular, we derived high-precision astrometry and multiband photometry of stars in NGC 416 and NGC 1978. The main results can be summarized as follows:

1. We identified distinct sequences of 1G and 2G stars along the red HB of 12 Milky Way GCs, NGC 416 in the SMC, and NGC 1978 in the LMC. These results confirm that MPs are a common feature of both Galactic and extragalactic GCs.
2. MPs along the red HB exhibit a high degree of variety, with the extension of the 1G and 2G sequences, the number of subpopulations, and the relative numbers of stars in each population changing from one cluster to another.
3. We measured the fraction of 1G stars of 14 GCs. This is the first time that this quantity is inferred in a large sample of clusters, homogeneously analyzed by using the red HB and the red clump. The fraction of 1G stars in Milky Way clusters ranges from ∼18% in the massive GC NGC 6388 ($\sim 1.1 \times 10^6 M_\odot$) to ∼68% in the low-mass cluster NGC 6838 ($\sim 4.9 \times 10^4 M_\odot$). Noticeably, by using HB stars, it was possible for the first time to measure the population ratios in NGC 5927, NGC 6304, and NGC 6441. We combined our results based on HB stars with previous findings based on MS and RGB stars, thus deriving improved estimates of the fractions of 1G and 2G stars in GCs.
4. The 1G fractions derived from red HB stars correlate with the present-day and the initial mass of the host cluster, with massive GCs having a larger fraction of 2G stars. The conclusion is confirmed also when we extend the number of clusters by including literature determination of the fraction of 1G stars inferred from the RGB and the MS. Similarly, the $m_{F336W} - m_{F438W}$ color extension of red HB correlates with cluster mass. These facts confirm that the incidence and complexity of the MP phenomenon depend on GC mass (Milone et al. 2020a). There is no correlation between the fraction of 1G stars and the age of the host GC.
5. We combined results from HST photometry of stars in the innermost ∼2.′7 × 2.′7 region and from ground-based wide-field photometry from Stetson et al. (2019) to investigate the radial distributions of 1G and 2G stars identified along the red HBs of NGC 104, NGC 5927, NGC 6366, and NGC 6838. We find that 2G stars of NGC 5927 and NGC 104 are more centrally concentrated than the 1G, whereas the two stellar populations of NGC 6366 and NGC 6838 share similar radial distributions. The 1G and 2G stars of the remaining clusters are consistent with the same radial distribution within the HST FoV, except for NGC 416, which is consistent with a more centrally concentrated 2G.
6. We discovered that GCs typically exhibit extended sequences of 1G stars along the red HB. NGC 6388 is the most extreme case and shows a more extended 1G sequence in the $m_{F336W} - m_{F438W}$ versus $m_{F275W} - m_{F336W}$ two-color diagram, when compared with NGC 6441, which is considered its "twin" cluster. By comparing the observed magnitude width of 1G stars

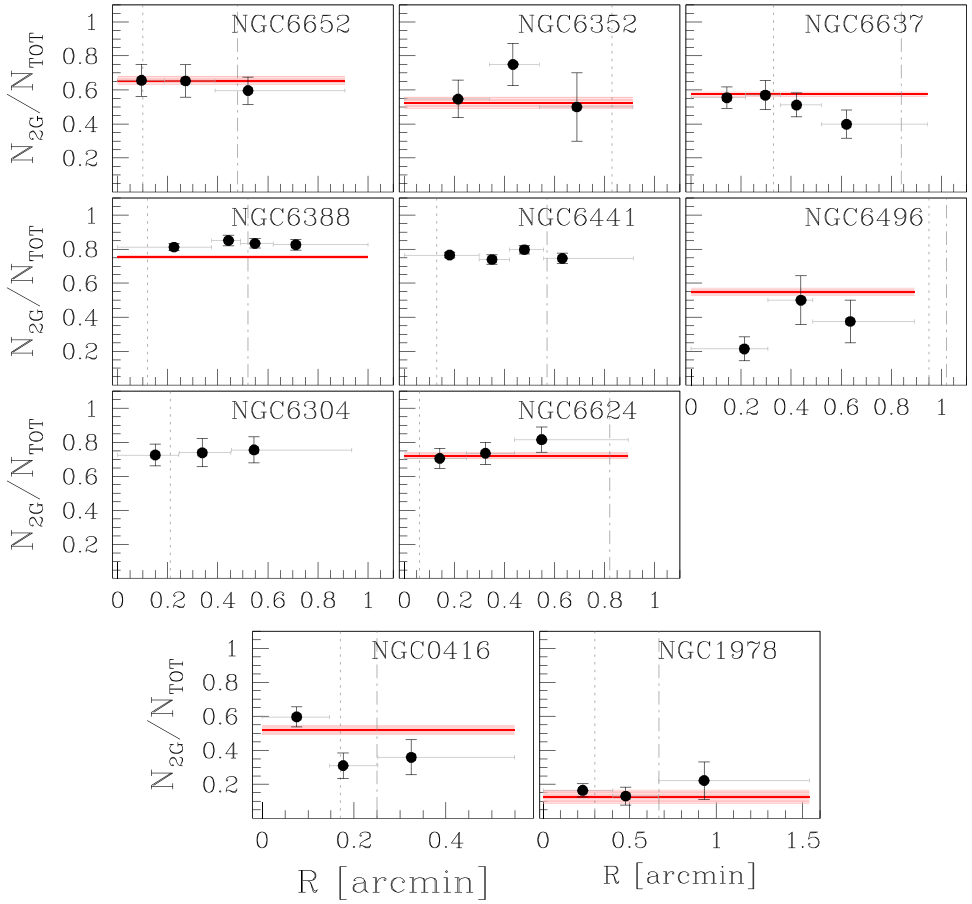

Figure 20. Same as Figure 19, but for the Galactic GCs NGC 6304, NGC 6352, NGC 6388, NGC 6441, NGC 6496, NGC 6624, and NGC 6652, and for the Magellanic Cloud clusters NGC 416 and NGC 1978.

Table 5
Probability that the Observed Radial Distribution of N_{2G}/N_{TOT} is Produced by a Flat Distribution

Cluster	p value
NGC 0104	<0.01
NGC 5927	<0.01
NGC 6304	0.99
NGC 6352	0.60
NGC 6366	0.75
NGC 6388	0.87
NGC 6441	0.59
NGC 6496	0.29
NGC 6624	0.71
NGC 6637	0.60
NGC 6652	0.96
NGC 6838	0.97
NGC 1978	0.89
NGC 0416	0.02

along the red HB with simulated HBs with the appropriate chemical composition, we find that the extension of the HB sequence of 1G stars is consistent with an internal spread in either helium or metallicity. Furthermore, the color extensions of the 1G sequence along the red HB and the RGB correlate with each other, thus suggesting that the extended 1G sequences in the ChM of RGB stars and in the two-color diagrams of red HB stars are associated with the same physical process.

7. The fraction of 1G stars in the extragalactic clusters NGC 416 and NGC 1978 are ∼0.55 and ∼0.85, respectively, and are larger than those of Galactic GCs with similar masses, which are typically dominated by the 2G. This finding corroborates previous evidence that the environment may affect the MP phenomenon. These results are consistent with a scenario in which the GCs are dominated by the 1G at formation, and most 1G stars are stripped away from the cluster due to interaction with the host galaxy. Indeed, in this scenario, we expect that the studied LMC and SMC clusters, which are younger than Milky Way GCs, are still dominated by the 1G. Moreover, due to their relatively small masses, the Magellanic Clouds would be less efficient than the Milky Way in stripping 1G stars from their GCs.

We thank H. Baumgardt and M. Hilker for providing the initial masses of GCs. This work has received funding from the European Research Council (ERC) under the European Union's Horizon 2020 research innovation program (grant Agreement ERC-StG 2016, No 716082 "GALFOR," PI: Milone, http://progetti.dfa.unipd.it/GALFOR), and the European Union's Horizon 2020 research and innovation program under the Marie Sklodowska-Curie (grant agreement No. 797100). E.D., A.P.M., and M.T. have been supported by MIUR under PRIN program 2017Z2HSMF (PI: Bedin). A.P. M. acknowledges support from MIUR through the FARE project R164RM93XW SEMPLICE (PI: Milone).

ORCID iDs

E. Dondoglio https://orcid.org/0000-0001-8415-8531
A. P. Milone https://orcid.org/0000-0001-7506-930X
E. P. Lagioia https://orcid.org/0000-0003-1713-0082
A. F. Marino https://orcid.org/0000-0002-1276-5487
M. Tailo https://orcid.org/0000-0002-1128-098X
G. Cordoni https://orcid.org/0000-0002-7690-7683
S. Jang https://orcid.org/0000-0002-1562-7557
M. Carlos https://orcid.org/0000-0003-1757-6666

References

Afşar, M., Sneden, C., Wood, M. P., et al. 2018, ApJ, 865, 44
Anderson, J., Sarajedini, A., Bedin, L. R., et al. 2008, AJ, 135, 2055
Baumgardt, H., & Hilker, M. 2018, MNRAS, 478, 1520
Baumgardt, H., Hilker, M., Sollima, A., & Bellini, A. 2019, MNRAS, 482, 5138
Bedin, L. R., Cassisi, S., Castelli, F., et al. 2005, MNRAS, 357, 1038
Bedin, L. R., Salaris, M., Piotto, G., et al. 2009, ApJ, 697, 965
Bellini, A., Anderson, J., & Bedin, L. R. 2011, PASP, 123, 622
Bellini, A., & Bedin, L. R. 2009, PASP, 121, 1419
Bellini, A., Piotto, G., Bedin, L. R., et al. 2009, A&A, 507, 1393
Bellini, A., Piotto, G., Milone, A. P., et al. 2013, ApJ, 765, 32
Carretta, E., Bragaglia, A., Gratton, R., & Lucatello, S. 2009, A&A, 505, 139
Castelli, F. 2005, MSAIS, 8, 25
Chantereau, W., Salaris, M., Bastian, N., & Martocchia, S. 2019, MNRAS, 484, 5236
Choi, J., Dotter, A., Conroy, C., et al. 2016, ApJ, 823, 102
Cordero, M. J., Pilachowski, C. A., Johnson, C. I., et al. 2014, ApJ, 780, 94
Cordoni, G., Milone, A. P., Marino, A. F., et al. 2018, ApJ, 869, 139
Cordoni, G., Milone, A. P., Mastrobuono-Battisti, A., et al. 2020, ApJ, 889, 18
Dalessandro, E., Mucciarelli, A., Bellazzini, M., et al. 2018, ApJ, 864, 33
D'Antona, F., & Caloi, V. 2008, MNRAS, 390, 693
D'Antona, F., Caloi, V., Montalbán, J., Ventura, P., & Gratton, R. 2002, A&A, 395, 69
D'Antona, F., Vesperini, E., D'Ercole, A., et al. 2016, MNRAS, 458, 2122
Dorman, B. 1992, ApJS, 80, 701
Dotter, A. 2016, ApJS, 222, 8
Dotter, A., Sarajedini, A., Anderson, J., et al. 2010, ApJ, 708, 698
Fischer, P., Welch, D. L., & Mateo, M. 1992, AJ, 104, 1086
Gaia Collaboration, Brown, A. G. A., Vallenari, A., et al. 2018, A&A, 616, A1
Glatt, K., Grebel, E. K., Gallagher, J. S. I., et al. 2009, AJ, 138, 1403
Glatt, K., Grebel, E. K., Jordi, K., et al. 2011, AJ, 142, 36
Goudfrooij, P., Girardi, L., Kozhurina-Platais, V., et al. 2014, ApJ, 797, 35
Gratton, R. G., Lucatello, S., Carretta, E., et al. 2011, A&A, 534, A123
Harris, W. E. 1996, AJ, 112, 1487
Icko Iben, I. J., & Rood, R. T. 1970, ApJ, 161, 587
Kraft, R. P. 1994, PASP, 106, 553
Kurucz, R. 2005, MSAIS, 8, 14
Kurucz, R. L. 1970, SAOSR, 309
Kurucz, R. L., & Avrett, E. H. 1981, SAOSR, 391
Kurucz, R. 1993, SYNTHE Spectrum Synthesis Programs and Line Data. Kurucz CD-ROM No. 18 (Cambridge, MA: Smithsonian Astrophysical Observatory)
Lagioia, E. P., Milone, A. P., Marino, A. F., et al. 2018, MNRAS, 475, 4088
Lagioia, E. P., Milone, A. P., Marino, A. F., Cordoni, G., & Tailo, M. 2019a, AJ, 158, 202
Lagioia, E. P., Milone, A. P., Marino, A. F., & Dotter, A. 2019b, ApJ, 871, 140
Lee, J.-W. 2017, ApJ, 844, 77
Lee, J.-W. 2018, ApJS, 238, 24
Lee, J.-W. 2019, ApJL, 875, L27
Lee, J.-W., & Sneden, C. 2020, arXiv:2006.01274
Lindegren, L., Hernández, J., Bombrun, A., et al. 2018, A&A, 616, A2
Marino, A. F., Milone, A. P., Przybilla, N., et al. 2014, MNRAS, 437, 1609
Marino, A. F., Milone, A. P., Renzini, A., et al. 2019a, MNRAS, 487, 3815
Marino, A. F., Milone, A. P., Sills, A., et al. 2019b, ApJ, 887, 91
Marino, A. F., Villanova, S., Milone, A. P., et al. 2011, ApJL, 730, L16
Marino, A. F., Villanova, S., Piotto, G., et al. 2008, A&A, 490, 625
Martocchia, S., Cabrera-Ziri, I., Lardo, C., et al. 2018a, MNRAS, 473, 2688
Martocchia, S., Niederhofer, F., Dalessandro, E., et al. 2018b, MNRAS, 477, 4696
Mateo, M. 1987, ApJL, 323, L41
McLaughlin, D. E., & van der Marel, R. P. 2005, ApJS, 161, 304
Milone, A. P., Bedin, L. R., Piotto, G., & Anderson, J. 2009, A&A, 497, 755
Milone, A. P., Marino, A. F., Bedin, L. R., et al. 2016, MNRAS, 455, 3009
Milone, A. P., Marino, A. F., Da Costa, G. S., et al. 2020a, MNRAS, 491, 515
Milone, A. P., Marino, A. F., Dotter, A., et al. 2014, ApJ, 785, 21
Milone, A. P., Marino, A. F., Mastrobuono-Battisti, A., & Lagioia, E. P. 2018a, MNRAS, 479, 5005
Milone, A. P., Marino, A. F., Piotto, G., et al. 2013, ApJ, 767, 120
Milone, A. P., Marino, A. F., Piotto, G., et al. 2015, ApJ, 808, 51
Milone, A. P., Marino, A. F., Renzini, A., et al. 2018b, MNRAS, 481, 5098
Milone, A. P., Piotto, G., Bedin, L. R., et al. 2012, ApJ, 744, 58
Milone, A. P., Piotto, G., Bedin, L. R., et al. 2012, A&A, 540, A16
Milone, A. P., Piotto, G., Renzini, A., et al. 2017, MNRAS, 464, 3636
Milone, A. P., Vesperini, E., Marino, A. F., et al. 2020b, MNRAS, 492, 5457
Monelli, M., Milone, A. P., Stetson, P. B., et al. 2013, MNRAS, 431, 2126
Niederhofer, F., Bastian, N., Kozhurina-Platais, V., et al. 2017, MNRAS, 465, 4159
Norris, J., & Freeman, K. C. 1982, ApJ, 254, 143
Paxton, B., Bildsten, L., Dotter, A., et al. 2011, ApJS, 192, 3
Paxton, B., Cantiello, M., Arras, P., et al. 2013, ApJS, 208, 4
Paxton, B., Marchant, P., Schwab, J., et al. 2015, ApJS, 220, 15
Renzini, A., D'Antona, F., Cassisi, S., et al. 2015, MNRAS, 454, 4197
Rich, R. M., Sosin, C., Djorgovski, S. G., et al. 1997, ApJL, 484, L25
Sabbi, E., Lennon, D. J., Anderson, J., et al. 2016, ApJS, 222, 11
Salaris, M., Cassisi, S., & Pietrinferni, A. 2008, ApJL, 678, L25
Salpeter, E. E. 1955, ApJ, 121, 161
SAS Institute Inc. Staff, C. 1988, SAS-STAT User's Guide: Release 6.03 Edition (USA: SAS Institute Inc.)
Sbordone, L., Bonifacio, P., & Castelli, F. 2007, in IAU Symp. 239, Convection in Astrophysics, ed. F. Kupka, I. Roxburgh, & K. L. Chan (Cambridge: Cambridge Univ. Press), 71
Sbordone, L., Bonifacio, P., Castelli, F., & Kurucz, R. L. 2004, MSAIS, 5, 93
Sbordone, L., Salaris, M., Weiss, A., & Cassisi, S. 2011, A&A, 534, A9
Smith, G. H., & Penny, A. J. 1989, AJ, 97, 1397
Sollima, A., Ferraro, F. R., Bellazzini, M., et al. 2007, ApJ, 654, 915
Stetson, P. B. 2005, PASP, 117, 563
Stetson, P. B., Pancino, E., Zocchi, A., Sanna, N., & Monelli, M. 2019, MNRAS, 485, 3042
Tailo, M., D'Antona, F., Caloi, V., et al. 2019a, MNRAS, 486, 5895
Tailo, M., D'Antona, F., Milone, A. P., et al. 2017, MNRAS, 465, 1046
Tailo, M., Di Criscienzo, M., D'Antona, F., Caloi, V., & Ventura, P. 2016, MNRAS, 457, 4525
Tailo, M., Milone, A. P., Lagioia, E. P., et al. 2020, MNRAS, 498, 5745
Tailo, M., Milone, A. P., Marino, A. F., et al. 2019b, ApJ, 873, 123
Zennaro, M., Milone, A. P., Marino, A. F., et al. 2019, MNRAS, 487, 3239